Tampere University

ABBA SALEH

Supercontinuum Lidar for Spectroscopic Sensing Applications

Tampere University Dissertations 849

Tampere University Dissertations 849

ABBA SALEH

Supercontinuum Lidar for Spectroscopic Sensing Applications

ACADEMIC DISSERTATION
To be presented, with the permission of
the Faculty of Engineering and Natural Sciences
of Tampere University,
for public discussion in the auditorium RG202
of the Rakennustalo, Korkeakoulunkatu 5, Tampere,
on 15 September 2023, at 12 o’clock.

ACADEMIC DISSERTATION
Tampere University, Faculty of Engineering and Natural Sciences
Finland

Responsible supervisor and Custos	Professsor Juha Toivonen Tampere University Finland	
Pre-examiners	Professor Zeyad T. Alwahabi The University of Adelaide Australia	Professor Matthieu Roussey University of Eastern Finland Finland
Opponent	Associate Professor Florian Schmidt Umeå University Sweden	

The originality of this thesis has been checked using the Turnitin OriginalityCheck service.

Copyright ©2023 Abba Saleh

Cover design: Roihu Inc.

ISBN 978-952-03-3026-2 (print)
ISBN 978-952-03-3027-9 (pdf)
ISSN 2489-9860 (print)
ISSN 2490-0028 (pdf)
http://urn.fi/URN:ISBN:978-952-03-3027-9

HIILINEUTRAALI PAINOTUOTE
ClimateCalc CC-000025/FI
PunaMusta Printing

Carbon dioxide emissions from printing Tampere University dissertations have been compensated.

PunaMusta Oy – Yliopistopaino
Joensuu 2023

PREFACE

This work was carried out in Laboratory of Photonics, Applied Optics research group, of Tampere University. I sincerely acknowledge the financial support from the European Union, Finnish Foundation for Technology Promotion, SKR foundation and Academy of Finland Flagship (PREIN). I also acknowledge the technical support and collaboration with Valmet, VTT and NKT Photonics.

I am very grateful to my supervisor Prof. Juha Toivonen for the opportunity to partake in this endeavor, and for the guidance towards this thesis. I also thank my industrial supervisor Jaani Silvennoinen for the support, especially in organizing the industrial measurement campaigns. I extend my gratitude to Prof. Goëry Genty who has been integral in the development of the light sources and a source of fruitful scientific discussions. In that regard, I am also grateful to Dr. Piotr Ryczkowski. I also thank Dr. Patrick Bowen and other colleagues at NKT Photonics for the hospitality and support during my research visit.

I have been privileged with a friendly and conducive working atmosphere during this journey. For that, I would like to thank all the members of the SK1 corridor, SUPUVIR(A) family, volleyball and football teams, UKO(A), Finnish language buddies, and my office mate Zahra (A.K.A. cookie expert).

Finally, I want to express my sincere gratitude to my parents for the unconditional love and support, without which none of this would be possible, and Agatka for steadfastly supporting my dreams and brightening my days.

> *"Every story has an end, but an ending is just a new beginning."*
>
> – *Anonymous*

ABSTRACT

Light detection and ranging (lidar) is a well established optical remote sensing technique with varying applications including atmospheric, environmental, automotive and other industrial applications. Lidar generally employs a monochromatic light source, which typically restricts its measurement capability to one observable at a time. The advent of a broadband light source termed supercontinuum (SC), also known as "white laser", offers novel possibilities for simultaneous multispectral analysis owing to its broad spectral bandwidth and laser like properties such as spatial coherence.

This thesis presents a new lidar system employing spectrally tailored SC light sources. The system exploits differential absorption between specific wavelength bands of the SC spectrum, enabling the first experimental demonstration of real-time simultaneous monitoring of flue gas parameters (including aerosol particle distribution, water vapor temperature and concentration) in an industrial biomass boiler. In the context of combustion diagnostics, this is particularly of great interest as real-time analysis of flue gas parameters is central to the optimization of the process efficiency and reduction of pollutants emission.

The technique is extended towards a more generic hyperspectral remote sensing in the mid-infrared wavelength range, where molecules possess characteristic absorption features known as the molecular fingerprints. Robust hypersepctral identification of black plastic waste is demonstrated with the aid of a micro-electro-mechanical system (MEMS) tunbale Fabry-Pérot interferometer filter. This is significant for recycling processes, as detection of black plastics with conventional near infrared sensors is tedious due to their strong absorption.

The results reported herein demonstrate excellent versatility and unique capability of supercontinuum lidar for robust diagnosis in combustion units and other industrial environments. Opening up novel perspective for real-time 3D analysis of industrial processes and other hyperspectral sensing applications.

CONTENTS

ABBREVIATIONS AND SYMBOLS

ATMOS	atmospheric trace molecule spectroscopy database
Ch	channel
DAQ	data acquisition
DAS	direct absorption spectroscopy
DIAL	differential absorption lidar
DU	detection unit
FPGA	field programmable gate array
FPI	Fabry-Pérot interferometer
FTIR	Fourier transform infrared (spectroscopy or spectrometer)
HITRAN	high-resolution transmission molecular absorption database
lidar	light detection and ranging
MEMS	micro-electro-mechanical systems
MIR	middle (mid) infrared
NIR	near infrared
NIST	national institute of standards and technology database
PCF	photonics crystal fiber
PE	polyethylene
PP	polypropylene
SC	supercontinuum
SNR	signal-to-noise ratio
SRS	stimulated Raman scattering

TDLS	tunable diode laser spectroscopy
UV	ultraviolet
ZDW	zerodispersion wavelength
Δ	difference
∂	accuracy
I_O	initial intensity
I_R	reference sample intensity spectrum
I_S	sample intensity spectrum
L	ratio of aerosol backscattering to extinction coefficient
l	optical path length
N	number density
N_B	background noise
O	geometrical overlap function
P_o	initial optical power
R	measurement distance (range)
r	reflectance
S	measured signal
T	temperature or transmittance
W	logarithmic range corrected signal
α	extinction coefficient
α_{abs}	absorption coefficient
α_{sca}	scattering coefficient
β	backscattering coefficient
Γ	filter transmission function
σ	absorption cross section
τ	measurement time

ORIGINAL PUBLICATIONS

Publication I	A. Saleh, A. Aalto, P. Ryczkowski, G. Genty and J. Toivonen. “Short-range supercontinuum-based lidar for temperature profiling”. *Optics letters* 44.17 (2019), pp. 4223–4226.
Publication II	A. Saleh, P. Ryczkowski, G. Genty and J. Toivonen. “Supercontinuum lidar for industrial process analysis”. *Optics Express* 29.25 (2021), pp. 42082–42089.
Publication III	A. Saleh, M. Mekhrengin, T. Dönsberg, T. Kääriäinen, G. Genoud and J. Toivonen. “Mid-infrared hyperspectral sensor based on MEMS Fabry-Pérot interferometer for stand-off sensing applications”. *Scientific Reports* 12.1 (2022), pp. 1–6.
Publication IV	A. Saleh, K. Kalmankoski, G. Genty and J. Toivonen. “In-situ analysis of combustion aerosol using a supercontinuum lidar”. *Optics Express* 31.15 (2023), pp. 23889–23896.

Author’s contribution

The thesis comprises four peer-review publications related to the development of a novel supercontinuum lidar system for short range spectroscopic sensing applications. A brief description of all the publications along with the author’s contribution is stated below.

Publication I	This letter reports the first proof-of-concept demonstration of combustion thermometry by a supercontinuum lidar. J. Toivonen and A. Aalto planned the initial experiment and the supercontinuum source is developed by A. Aalto with the help of G. Genty. The final setup to perform the experiment is developed by the author with the help of P.

	Ryczkowski. The author conducted the experiments and analysed the data. The manuscript is prepared by the author with contributions from the co-authors.
Publication II	This work is the first experimental demonstration of real-time gas monitoring in an industrial process using a broadband supercontinuum lidar. The author planned the experiment with the assistance of P. Ryczkowski, performed all the measurements and analysed the data. The author also prepared the manuscript, and all the co-authors contributed to finalizing the publication.
Publication III	This publication reports a robust mid-infrared hyperspectral sensor for novel stand-off sensing applications. The initial experiment is planned by G. Genoud, M. Mekhrengin, T. Dönsberg and T. Kääriäinen. The author contributed to the development of the final working setup, conducted all the measurements and analysed the data with contributions from the co-authors. The author prepared the manuscript, while all the co-authors contributed to finalizing the paper.
Publication IV	This work presents the first proof-of-concept demonstration of real-time analysis of combustion aerosol in a full-scale industrial boiler by a supercontinuum lidar system. The supercontinuum is developed by the author with the help G. Genty. The author built the laser system and optical setup and performed all the measurements. The real time data collection and pre-processing system was designed and implemented by K. Kalmankoski. The data was analysed by the author and K. Kalmankoski. The author prepared the manuscript along with contributions from the co-authors.

1

Introduction

REMOTE sensing is an integral part of the sensory system of most, if not all, living organisms. At least three of the basic human senses including sight, hearing and smell execute their function remotely. The sense of sight is arguably the most exceptional as it provides us with the richest information regarding our surrounding. The functionality of the human eye is analogous to optical remote sensing. Although the eye uses the visible part of the electromagnetic radiation, optical remote sensors cover a much broader spectral bandwidth ranging from the deep ultraviolet to far infrared spectrum of the electromagnetic radiation, thereby avails one significantly more information. For instance, infrared cameras and other night vision devices use infrared wavelength to enable vision in the dark or low visible light conditions, where vision with the human eye is otherwise infeasible. Beside mimicking visual sensing and representations, the interaction of light with matter can lead to various other physical phenomena. Yielding more unique and diverse information essential to understanding the physical world.

Although, to exploit these physical phenomena, some remote optical sensors rely on natural light source in the environment for target illumination, most sensors utilize active light sources like lasers. The very low divergence of a laser beam allows it to be collimated over long distances, making it very attractive for remote sensing applications. One of the most common optical remote sensing technique employing a laser as a primary transmitter is known as light detection and ranging (lidar). It measures backscattered light from a transmitted laser beam with very high range resolution. Enabling it to extract localized information about a probed volume, stretching over several kilometers, which is otherwise physically inaccessible. Lidar is a well established technique in the atmospheric research community, where it has been used to monitor and characterize e.g. temperature [1–3], wind speed [4] as well as molecular [5] and particulate species [6]. Other applications include topographic mapping of land [7] and oceans [8], vegetation monitoring in forestry [9] and other environmental monitoring [10]. Lidar also lends itself to short range applications in cultural heritage preservation [11], agriculture [12] and other industrial applications, to name a few. It also recently gain significant attention for consumer devices such as mobile phone cameras and autonomous driving.

Lidar have also begun to gain traction as a diagnostic tool for industrial process analysis, especially in combustion power plants like boilers. The ever increasing need for renewable energy alternatives, to address the environmental concerns associated with energy production, have reinvigorated interest in combustion schemes utilizing renewable fuels like biomass owing to its CO_2 neutrality [13]. Additionally, biomass fuels are cheap and abundant as they are by-products of other processes, thereby comprise a varying degree of composition. The inhomogeneous fuel composition can often lead to certain adverse effects and inefficiencies, compelling operators to compromise standard process routines which consequently undermines process efficiency [14]. Therefore, novel control measures and innovations for monitoring of localized flue gas parameters including temperature, molecular concentrations and fly ash aerosol particles are essential for optimal performances. The dynamic and high temperature conditions associated with combustion processes challenges the traditional analysis techniques. Another bottleneck is the limited optical access in power plant boilers, which complicates the use of other optical spectroscopic solutions. In this context, the remote measurement capability and other aforementioned features of a lidar makes it an extremely viable candidate solution. Various lidar methods have been proposed for combustion diagnostics [15–18]. However, lidar typically employs light sources that are narrow band, thereby restricting it to measurement of one parameter at a time.

Recent advances in fiber optics and laser technologies have led to the development of broadband light sources with laser-like characteristics known as supercontinuum [19]. Making it feasible to develop compact and cheap light sources with broad spectral bandwidth [20]. This offers novel possibilities for the development of a broadband lidar system with real-time simultaneous multi-specie sensing capability.

1.1 Research objective and scope of the thesis

The overall objective of this thesis is to develop a novel broadband lidar system for short range spectroscopic sensing applications, and demonstrate proof-of-concept in both laboratory and industrial measurement context. Therefore, the work in this thesis is mainly experimental in nature.

The specific research questions of this thesis are briefly summarized as follows:

- Is the supercontinuum lidar technique experimentally realizable?
- Is it suitable for high temperature and dynamic environments?
- How does it perform compared to existing methods?
- Is the technique implementable in full-scale industrial measurement context?
- Can the technique be extended to versatile hyperspectral sensing in the mid-infrared?

All the outlined research questions have been thoroughly investigated via rigorous literature and experimental inquiries in conjunction with numerical and theoretical studies. The results are published in peer-review scientific journals (**Publication I to IV**) listed in the appendices. Further development of the supercontinuum lidar especially in terms of optimization and miniaturization is currently underway as this thesis is being written.

2

Absorption spectroscopy

This chapter introduces absorption spectroscopy as an experimental science. And briefly discusses the origin of the so called absorption lines in a spectrum and the specific associated transitions, and how they play a central role in the analysis of atomic and molecular specie in a sample.

2.1 Background

The study of the interaction between matter and electromagnetic radiation is referred to as optical spectroscopy. This interaction exhibits various physical phenomena including scattering, reflection, transmission, emission, and absorption. The consequent distribution of the radiation intensity with respect to frequency or wavelength, i.e. the spectrum associated with any of these phenomena, encodes atoms or molecules specific signatures. Making these interactions individually capable of serving as the basis for their respective spectroscopies. In this context, absorption spectroscopy relies on absorption as the main approach to extract information regarding an investigated matter.

The earliest reported spectroscopy experiment can be dated back to the famous 1665 Newton's dispersion of white light [21]. Where he spatially separated the various wavelengths (colors) of the visible part of the solar radiation using a triangular glass prism. Upon further analysis of the visible solar spectrum in the early 1800s, it was discovered that the spectrum consists of many dark lines, also known as the Fraunhofer lines. These lines represent selective absorption of the solar radiation by various gaseous elements in the sun atmosphere as shown in Figure 2.1.

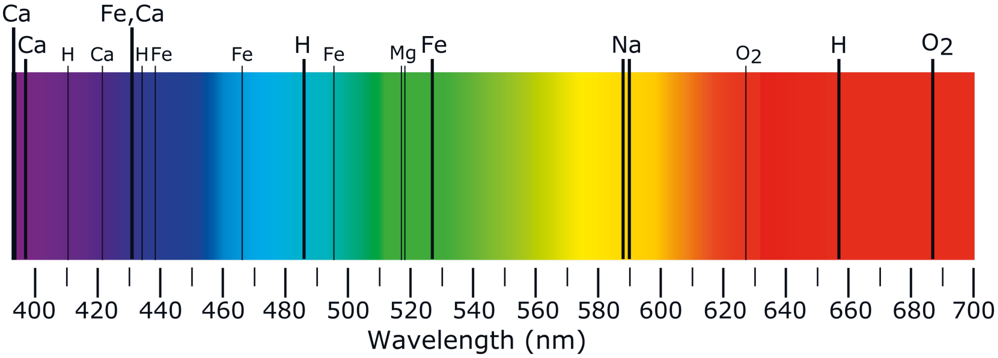

Figure 2.1 Visible solar spectrum with characteristic dark lines representing absorption by various elements present in the outer atmosphere of the sun.

This approach is analogous to the so called direct absorption spectroscopy (DAS) technique, which is the simplest and the most basic method for absorption spectroscopy. A simple demonstration of DAS typically involves shining a laser light through a cell containing liquid or gaseous samples and measuring the output intensity. The light experiences exponential attenuation governed by absorption at the laser wavelength, which is proportional to the parameters of the sample as stated by the Beer-Lambert law [22]

$$I(\lambda) = I_0(\lambda)\exp\{-N\sigma(\lambda)l\}, \tag{2.1}$$

where $I_0(\lambda)$ is the incident intensity, N is the number density of the absorbers, $\sigma(\lambda)$ is the wavelength dependent absorption cross section and l is the optical path length (i.e., length of the absorbing medium). The absorption cross section further depends on other parameters such as temperature. This effect is more active in high temperature conditions as discussed in Chapter 3. The probability of the laser light being absorbed by the sample is also governed by the absorption cross section, which can be determined experimentally or modeled using quantum mechanical perspective of light matter interaction [23].

2.2 Absorption spectroscopic transitions

The process of absorption involves transition of atoms or molecules from a lower energy state to a higher energy state. Thus, absorption occurs when the transition energy between the states matches the frequency of the electromagnetic radiation, i.e. resonance, resulting in the so called absorption line in a spectrum. For absorption process involving atoms, the quantized energy states are defined by the distribution of electrons in the atomic or molecular orbitals. Yielding unique energy states structure, for individual elements, with specific sets of electronic transitions permitted between them. Observation of electronic absorption lines requires high energy photon, typically in the ultraviolet and visible region of the electromagnetic spectrum, due to the large energy difference between the electronic states.

On the other hand the absorption spectra of molecules comprises additional energy states attributed to their nuclear motions, such as rotation and vibration, which makes it rather tedious in comparison to the aforementioned atomic absorption spectra. Therefore, in addition to electronic states, molecules also have quantized energy states associated with their modes of rotation and vibration as described below.

Vibrational transitions require less energy compared to electronic transitions as the separation between the vibrational energy levels is smaller. Hence, excitation of vibrational modes typically occur in the infrared spectral region. Specific forms of vibrational absorption lines are present in different portion of the infrared spectrum. In the mid-infrared, vibrational transition mainly involves excitation from a ground state to the first excited state, which is also known as fundamental transition. Whereas the near infrared allows excitation to higher energy states as well as simultaneous excitation of more than one vibrational mode. Thus, the names overtone and combination transitions for the former and latter, respectively.

Rotational transitions require even smaller photon energy, as the rotational energy levels are more densely packed. This is why rotational lines are typically observed in the microwave spectral region. Figure 2.2 shows an example of energy level system with arrows indicating pure electronic, vibrational and rotational transitions.

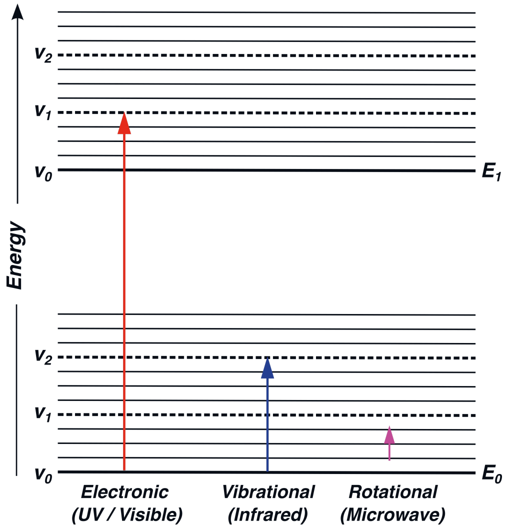

Figure 2.2 Energy level diagram with arrows indicating pure electronic, vibrational and rotational transitions. E_0 and E_1 are the ground and first excited electronic states, respectively. The vibrational states are represented by v and the rotational states are the densely packed thin lines within the vibrational states.

Besides the aforementioned pure transitions, other complex excitations take place in the infrared. For instance, absorption of infrared photons can induce both rotational and vibrational transitions in a molecule. Exciting the molecule to a higher vibrational state while the final rotational state is subject to the selection rule of the molecule, which defines the allowed transition between two quantum mechanical states. This kind of transition is also referred to as rotational-vibrational transition or simply as ro-vibrational transition. The absorption line of such transitions typically compose of a band structure rather than a line. And the pure vibrational transition is located at the center of the band, whereas the side branches corresponds to the accompanying rotational transitions. Similarly, electronic transitions can be followed by vibrational and rotational transitions and this kind of transition is termed rovibronic or rotational-vibrational-electronic transition. The absorption spectra investigated in this thesis are mainly associated with ro-vibrational and pure vibrational transitions.

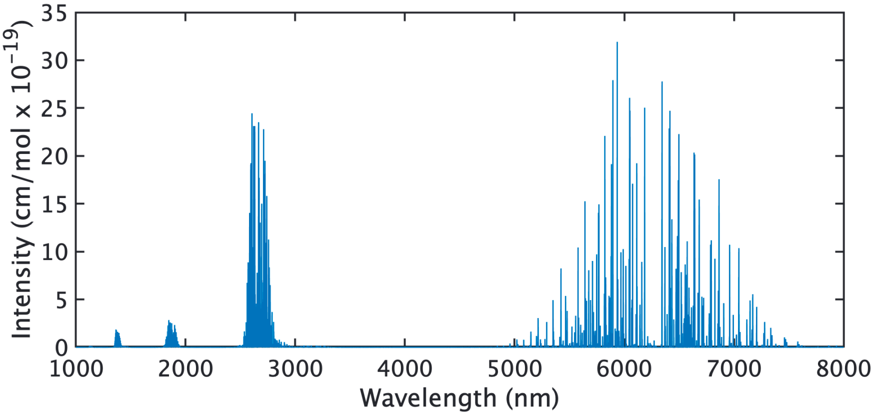

Figure 2.3 Spectral line intensity of water vapor covering transitions in the near to mid infrared spectral region.

2.3 Infrared absorption band intensities

The strength of an absorption process is defined by the transition intensity, which is subject to the change in dipole moment of the molecule involved with the vibrational transition [24]. Generally, molecules demonstrate strong fundamental vibrational transitions in the infrared, hence, the term molecular fingerprint region. And the weaker bands in the near infrared are attributed to combination and overtone transitions. Figure 2.3 presents water vapor (H_2O) spectral line intensity modeled using the HITRAN database [25]. One can see that the line intensity around 1000 – 2000 nm region is orders of magnitude lower than that around 6000 nm. Although HITRAN is used for the water vapor intensity spectrum, other similar databases including NIST [26], ATMOS [27], PNNL [28], GEISA [29], and HITEMP [30] are also available. More information about modeling molecular spectra using these databases can be found in Ref. [25].

3
Lidar

THIS chapter introduces light detection and ranging (lidar) and its operational principle. It also presents a brief overview of various lidar techniques relevant to this thesis, which sets the framework of the work reported in the subsequent chapters.

3.1 Background

Lidar is a remote sensing technique which operationally relies on the measurement of backscattered optical frequency electromagnetic radiation [31]. Hence, the acronym lidar meaning "light detection and ranging". It is also referred to as "laser radar" owing to its similar functionality to radar, which operates in the radio frequency. The invention of laser was the main prelude to lidar development due to the peculiar properties of laser beams such as high intensity and very low divergence. The very high spatial coherence allows the beam to be collimated over very long distances, enabling remote sensing applications in various fields including forestry, astronomy, autonomous driving, atmospheric and environmental monitoring, and other industrial applications.

A lidar unit can be broadly divided into a transmitting and a receiving unit. The transmitter comprises a laser, collimation optics and sometimes a beam expander, while the receiver composes of the receiving optics and a detection unit. The transmitter and receiver are generally combined as a single unit which is also known as a transceiver. A simple lidar transceiver typically operates by shining a laser light pulse to a target, and measuring the time of flight of the backscattered light pulse upon incidence on the detector. The measured backscattered light can be expressed as [31]

$$P(R,\lambda) = P_0(\lambda)\beta(R,\lambda)\frac{O(R)}{R^2}e^{-2\int_0^R \alpha(\lambda,R')\,dR'}, \tag{3.1}$$

where $P_0(\lambda)$ is the initial power spectrum of the light source, $\beta(R,\lambda)$ is the backscattering probability of the target, R is the distance traveled by the backscattered light pulse during the time of flight, $O(R)$ is the geometrical overlap function of the laser beam and the receiver field of view. The backscattered light further experiences exponential attenuation governed by the specific form of the Beer–Lambert law for lidar. $\alpha(\lambda, R')$ is the extinction coefficient and is subject to the physical phenomena (e.g., scattering and absorption) at play. Thus, various physical phenomena can be exploited depending on the application. Note that a measured lidar return typically comprises background contribution in addition to the lidar signal described above. The lidar equation presented in Equation 3.1 is used throughout this thesis with minor modifications in some specific cases.

3.2 Lidar techniques

Although there are several interesting lidar techniques, the discussion herein is limited to techniques relevant and complementary to the novel supercontinuum lidar developed in this thesis. More detailed description of various lidar techniques and their methodologies can be found in Refs. [31, 32].

Elastic-backscatter lidar exploits elastic scattering i.e., a scattering phenomenon where the wavelength of light remains unchanged. Its simplest demonstration involves transmitting a single wavelength laser to a target and measuring the elastically backscattered light. This type of lidar is widely used in atmospheric applications for aerosol analysis [33, 34] as well as cloud layers [35]. It is also extended to other 3D point cloud mappings in e.g. automotive sector for autonomous driving [36].

Doppler lidar probes motion of scatterers along the incident beam path. The interaction of the light with the scatterers Doppler-shifts the frequency of the incident light to a higher or lower value, depending on the direction of motion of the scatterers. The resulting shift in frequency is extremely small and could be measured directly using a set of narrow-band spectral filters. However, a coherent detection scheme, also known as heterodyne detection, is usually employed. This technique is commonly used for the measurement of wind speed [37–39].

Raman lidar takes advantage of the inelastic Raman scattering process, resulting in a change in the vibrational-rotaional state of a molecule. The scattering induces a shift in frequency, of the incident light, equal to the energy difference between initial and final states of the molecule. The intensity distribution of the Raman band is proportional to population of states through the Boltzmann distribution. Thus, encoding temperature information regarding the scattering volume. Raman lidar have been demonstrated for atmospheric temperature profiling [40–43].

Fluorescence lidar technique utilizes fluorescence process, which involves exciting molecules or atoms by an incident photon to a higher energy level followed by a subsequent relaxation via spontaneous emission. Fluorescence lidar have been routinely used for studying cultural heritage [11, 44] as well as the environment [45, 46].

Differential absorption lidar (DIAL) employs two single wavelengths or narrow-band lasers, e.g. tunable diode lasers, corresponding to different absorption characteristic of the target of interest. Where one spectral channel is absorbing and the other is off resonance. Taking the ratio of the backscattered signal of the respective channels enables measurement of e.g., concentration of molecular specie with relatively high sensitivity. The ratio also cancels out the coefficients of the lidar return of both channels, making it a self calibrating technique. DIAL is commonly used for the measurement atmospheric trace gas concentration [47–50]. Besides the atmospheric applications, DIAL also lends itself to environmental monitoring [51] and other short range industrial applications.

3.3 Supercontinuum light source

Conventional lidar techniques require the incident laser line-width to be precisely in tune with the specific wavelength associated with the exploited physical phenomena, thus, restricting them to the measurement of one specie at a time. The advent of a broadband light source, with laser-like properties, termed supercontinuum, offers novel perspective for a robust lidar technique capable of simultaneous multi-specie analysis. This section briefly discusses the history regarding the origin of supercontinuum and, the various mechanisms involved in supercontinuum generation. This set the stage for the development of the various light sources which played a key role in realization of the subsequently reported supercontinuum lidar.

A supercontinuum (SC) is generated when a narrow line-width laser experiences a dramatic broadening upon propagation through a nonlinear medium. The first observation of such phenomenon can be dated back to the 1970s work of Alfano et al. where they observed a continuous spectrum, spanning $400-700\,\mathrm{nm}$, after highly intense laser pulses were focused into a borosilicate glass [52]. In about a decade later the term supercontinuum was adopted [53], highlighting the extent of the broad spectral bandwidth generated as a consequence of the nonlinear propagation.

The nonlinear propagation is attributed to the nonlinear polarization of the medium by the incident electric field, which brings higher-order susceptibility into play. SC generation is mainly observed in materials with third-order nonlinear susceptibility, and the nonlinear dynamics are typically associated with the optical Kerr-effect. In this context, the advent of single mode optical fibers have paved the way for practical applications of supercontinuum owing to their unique ability to tightly confine highly intense optical field over significantly longer propagation distance. Thereby, enhancing nonlinear interactions as opposed to bulk materials in which light is prone to diffraction. The biggest milestone was the emergence of microstructured fibers known as photonics crystal fiber (PCF) [54], which allows tailoring the dispersive and nonlinear parameters of the fiber [55–57]. This led to the generation of first octave-spanning supercontinuum extending from the UV to NIR [58]. In addition to the significantly large spectral bandwidth, fiber based supercontinuum allows single mode operation, thus, enabling the generated SC to maintain the same spatial coherence as the pump laser. This is extremely attractive from a practical standpoint, as it enables collimation of the SC beam over longer distances.

The nonlinear dynamics underpinning the mechanism of supercontinuum generation in optical fibers can be coarsely categorized by the pulse duration (long and short) of the injected laser pulse and the dispersion regimes (normal and anomalous) of the fiber. Although the short pulse (i.e., femtosecond) regime is central for the generation of interesting coherent SC sources, most of the commercially available lasers operate in the long pulse (i.e., picosecond to nanosecond) regime and as continuous wave. Hence, making the long pulse regime extremely crucial from applications viewpoint. All the SC sources in this work are generated using long pump pulses, therefore, the following discussion is restricted to SC generation in the long pulse regime.

In the normal dispersion regime SC generation by long pump pulses is governed by stimulated Raman scattering (SRS), extending the spectrum towards the long wavelength range via energy transfer from the pump pulse to the Stokes Raman. The Stokes waves are subsequently amplified, essentially acting as a pump triggering new SRS process. This leads to cascaded SRS process extending the spectrum asymmetrically towards the long wavelength range [59, 60]. The SC sources in the work presented in **Publication I and II** are generated via this process.

In the anomalous dispersion regime modulation instability is triggered by the input noise, thus, breaking the long pump pulses into a large number of solitons with random features in terms of duration and amplitude [61]. If the pump wavelength is close to the zerodispersion wavelength (ZDW) of the fiber, the spectrum extends towards the short wavelengths via dispersive waves triggered by solitons crossing into the normal regime. The solitons also trigger SRS which extends the spectrum towards the long wavelength. The SC sources in the work reported in **Publication III and IV** are generated via this process.

3.4 Supercontinuum lidar

This section presents a novel supercontinuum differential absorption lidar (SC-DIAL) exploiting the exotic features of tailored SC sources and, discuses its measurement principle. Its application to simultaneous analysis of flue gas parameters in combustion power plants is presented for the first time. The results of this work are reported in **Publication I, II and IV**.

The work reported here is among the earliest demonstration of a short-range supercontinuum lidar (SC-lidar) [62–64], and the first attempt to extending the technology to combustion diagnostics especially in waste or biomass powered boilers. The inhomogeneous nature of biomass fuel demands real-time monitoring of flue gas parameters for feedback and control, to enable optimal performance of the combustion process. For this purpose, thermocouple probe [65] and Fourier transform infrared (FTIR) spectroscopy [66, 67] have been conventionally employed to obtain temperature and molecular concentration information, respectively. These probes are typically intrusive, slow and point-wise in nature, making them complex for in-situ monitoring of the dynamic flue gas parameters. Further, the low penetration depth of the thermocouple limits its measurements to the proximity of the furnace wall. This makes it prone to thermal radiation, and the measurement is also not representative of the rest of the furnace volume. In this context, the SC-DIAL presents a unique contribution to the field of combustion diagnostics. Where it competes with implemented solutions such as diode laser grids [68–72] and ultrasound [73, 74], and other advanced techniques including optical spectroscopic [75–82] and lidar [15–18] methods being researched for combustion diagnostics.

In principle, the methodology of SC-DIAL is analogous to that of a typical DIAL, however, the broad spectral bandwidth of the SC demands a special treatment of the SC-DIAL equations. The SC-DIAL takes advantage of the high temperature combustion process, which induces temperature dependent change in absorption of a probed species. The physical basis for this phenomenon is attributed to the effect of temperature on the population of higher excited ro-vibrational states, which alters the absorption spectrum and yields

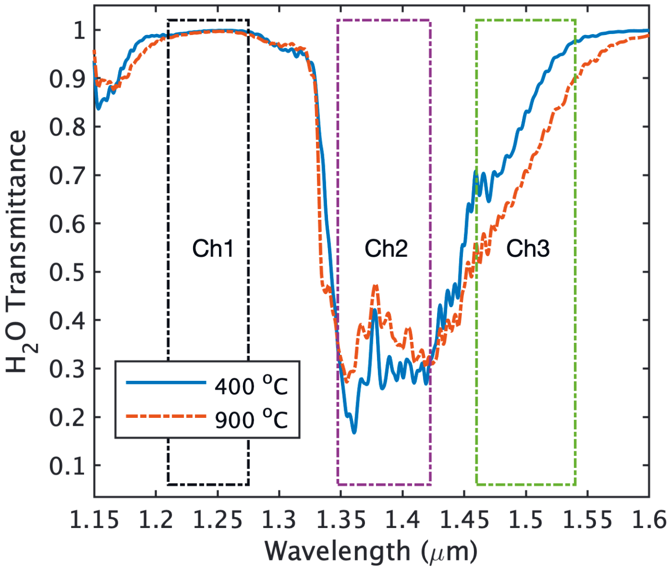

Figure 3.1 Modeled transmittance spectrum of water vapor, under specific boiler conditions, at typical extreme temperatures observed in the furnace. Overlay is the corresponding full width at half maximum (FWHM) of Channels 1, 2, and 3, respectively. **[Publication II]**

the so called "hot bands". We investigated the absorption spectrum of water vapor (H_2O), which is one of the primary flue gas component in power plant boilers, from one to eight micron to find suitable wavelength range comprising these hot bands. For this purpose, transmittance spectrum of H_2O under typical biomass boiler conditions is modeled with high spectral resolution using the HITEMP database [30]. The region between 1.2 μm and 1.6 μm was found to be the most suitable, which also coincides with the best range for detector choice. The resulting H_2O transmittance spectrum for this region, convoluted to low spectral resolution for better visualization, is presented in Figure 3.1. One can observe a characteristic temperature dependent transmission in three specific regions of the transmittance spectrum labeled Ch1, Ch2 and Ch3, respectively. The differential absorption spectrum can be exploited to deduce temperature by comparing the transmittance ratio between the different channels as described below.

The SC-DIAL measured backscattered signal for a given channel after a time of flight t_m can be expressed as

$$S_n(t_m) = \frac{O_m \beta_m}{{R_m}^2} \int_{\Delta\lambda_n} P_0(\lambda)\Gamma_n(\lambda) \exp\left[-2\sum_{k=1}^{m} N_k \sigma_k(\lambda, T)\Delta l_k\right] d\lambda, \tag{3.2}$$

where O_m is the SC-DIAL geometrical overlap factor, R_m is the distance traveled by the light pulse after a time of flight t_m, β_m is the backscattering coefficient and is considered to be wavelength independent as we utilize a very small wavelength range. Additionally, the primary scattering source in boilers is fly ash particles with much larger dimension than the wavelength of the light source. $P_0(\lambda)$ is the power spectrum of the SC source, $\Gamma_n(\lambda)$ is the filter transmission function for the channel $n = 1, 2, 3$ and $\Delta\lambda_n$ is the corresponding spectral width of a given channel. N_k is the molecular number density of the probed species and $\sigma_k(\lambda, T)$ is the temperature dependent absorption cross section. The path R_m traveled by the light pulse is split into discrete segments wherein the gas temperature and concentration is considered constant. The minimum length of a segment $\Delta l_k = \frac{\tau c}{2}$ is defined by the SC pulse duration τ (c is the speed of light). The parameters of the first segment are derived using initial spectrum of the light source. And calculation of the second segment transmission demands modification of the initial spectrum by the first segment absorption. Thus, the process is iteratively repeated as the absorption of all preceding segments is determined. The total transmittance of a given channel within a segment can be obtained from

$$T_{n,m} = \frac{S_n(t_{m+1})}{S_n(t_m)}, \tag{3.3}$$

where $S_n(t_{m+1})$ and $S_n(t_m)$ are the measured backscattered signal over time t_{m+1} and t_m, respectively. Taking the ratio of transmittance between two different channels cancels out the effect of the coefficient $\frac{O_m \beta_m}{{R_m}^2}$ on the signal. Meaning that knowing the filter transmission profile, initial SC source spectrum and the gas absorption cross section is sufficient to simulate the measured transmittance ratios. Using the HITEMP database, the simulated ratio is devised to comprise an array of values at varying temperatures and concentrations of the probed species. The species concentration and temperature values can be deduced by fitting the simulated ratios to the the measured ratios using

$$\Delta_{21,m} = \left|\frac{T_{2,m}}{T_{1,m}} - \frac{T_{2,Sim}}{T_{1,Sim}}\right| \tag{3.4}$$

$$\Delta_{31,m} = \left|\frac{T_{3,m}}{T_{1,m}} - \frac{T_{3,Sim}}{T_{1,Sim}}\right|, \tag{3.5}$$

where $\Delta_{21,m}$ and $\Delta_{31,m}$ are the numerically computed difference between the measured and simulated ratios. The concentration and temperature of the probed species corresponds to the point with minimum error solution.

4

Integrating path supercontinuum DIAL

This chapter discuses two key proof-of-concept demonstrations of the SC-DIAL measurement of average values of water vapor by integrating the total backscattered signal across the optical path. The approach considers the entire optical path, containing the gas specie, as a single segment. The first part of this chapter exploits the temperature dependent differential absorption between two channels to show thermometry in a laboratory furnace. The second part explores simultaneous analysis of water vapor temperature and concentration in an industrial power plant boiler.

4.1 Thermometry in a laboratory furnace

Proof-of-concept demonstration of the SC-DIAL thermometry in a laboratory furnace using two spectral channels is reported in **Publication I**. The experimental setup, which is reproduced from **Publication I**, is presented in

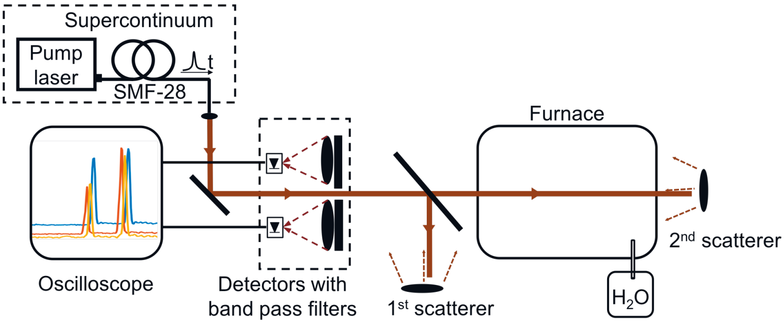

Figure 4.1 Experimental setup for the laboratory scale thermometry measurements by the supercontinuum lidar. **[Publication I]**

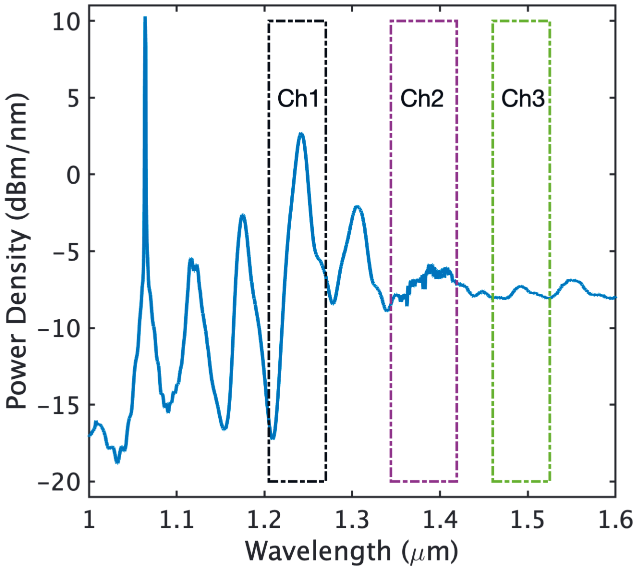

Figure 4.2 Power density spectrum of the supercontinuum. The dashed rectangles in the figure represents the FWHM of the bandpass filters for the respective spectral channels. **[Publication I]**

Figure 4.1. The SC is generated via a cascaded Raman process in a 500-m-long SMF-28 fiber, pumped by a Q-switched laser operating at 1064 nm producing 2-ns-long, 1 kW peak power pulses at a repetition rate of 280 kHz. The power spectral density of the generated SC is presented in Figure 4.2. The furnace temperature is remotely measured by probing, the temperature dependent differential absorption of water molecules, of Ch1 and Ch2 wavelength bands of the SC spectrum backsactteredby the two scatterers placed before and after the furnace.

Figure 4.3 (a) shows the resulting transmittance of individual channel across the 1-m-long furnace comprising 100 % H_2O. Ch1 shows negligible absorbance with increasing temperature, whereas Ch2 demonstrates a linear response with increasing temperature. The response of both channels is consistent with the modeled transmittance values. The furnace temperature is deduced by taking a ratio of Ch2 to Ch1 measured transmittance. The result is presented in Figure 4.3 (b), which is in excellent agreement with the simulated transmittance ratios. Yielding a temperature measurement accuracy of about 40 °C in

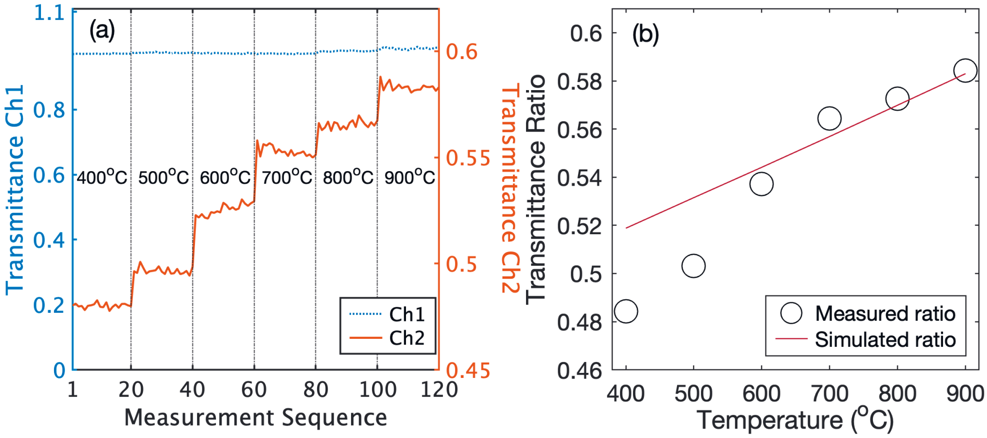

Figure 4.3 Measured water vapor parameters in a laboratory furnace. (a) Transmittance of Ch1 and Ch2 at varying furnace temperature (b) Transmittance ratio of Ch2 to Ch1 with respect to the furnace temperature. **[Publication I]**

the temperature range of 600 – 900 °C. The slight discrepancies at the lower temperature range is attributed to losses originating from condensation on the inlet window and nonuniform temperature distribution in the furnace. However, these challenges are somewhat nonexistent or negligible in industrial power plant boilers.

The results of this initial proof-of-concept measurements set the framework for real-time measurement in a full-scale industrial boiler. Opening up the possibility of extending the technique to probe additional parameters of the probed gas, like molecular concentrations, by utilizing additional spectral channels.

4.2 Combustion diagnostics in an industrial boiler

The work herein presents the first experimental demonstration of gas monitoring in an industrial process using a supercontinuum lidar system. The results of this work are presented in **Publication II**. The measurement campaign was conducted at a 9 meters wide bubbling fluidized bed (BFB) biomass boiler in Naistenlahti Tampere, Finland. The boiler has a thermal capacity of 190 MW and utilizes a fuel mixture comprising peat and wood. One of the few available openings on the boiler side wall was used to optically access the furnace.

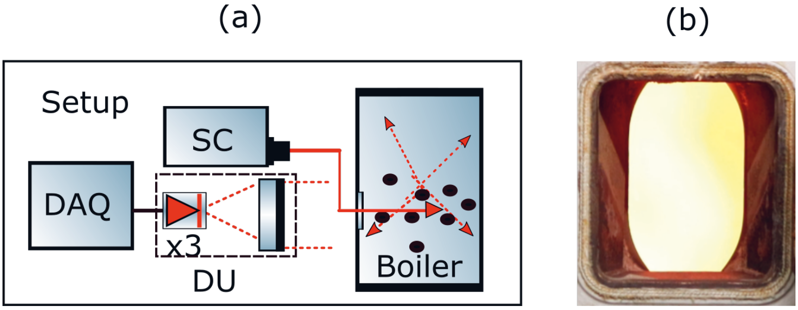

Figure 4.4 Industrial measurement arrangement. (a) Schematic representation of the experimental setup. (b) The opening hatch used as the inspection window.

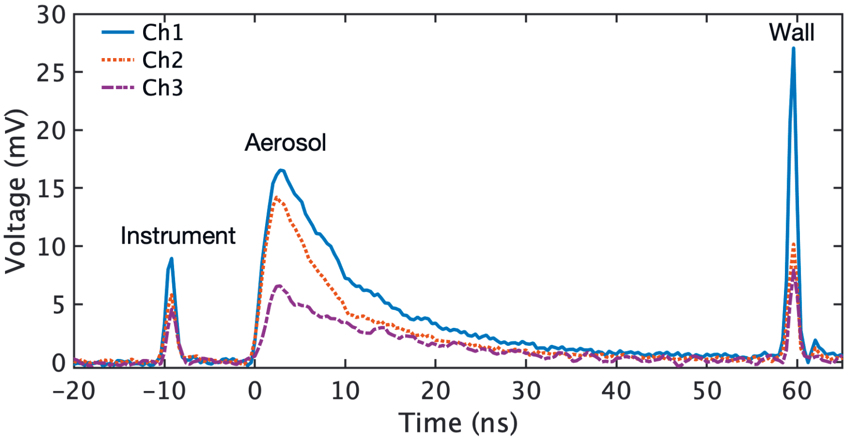

Figure 4.5 Measured Ch1(solid line), Ch2(dotted line) and Ch3 (dashed line) backscattered signal from an industrial power plant boiler. **[Publication II]**

Since H_2O concentration in the boiler is unknown and very dynamic, the measurement demands full use of the three spectral channels to simultaneously probe average temperature and concentration of H_2O across the furnace. The SC-DIAL collection optics is modified to be collinear for all the three channels, as opposed to the laboratory scale measurement, in order to enhance the collection efficiency across all the channels. Figure 4.4 (a) shows a schematic representation of the experimental setup for the industrial measurement, and Figure 4.4 (b) shows the opening hatch used as the optical access. Note that the noise associated with the continuous thermal radiation, seen from the hatch picture in Figure 4.4 (b), is negligible compared to the instantaneous peak power of the SC pulses.

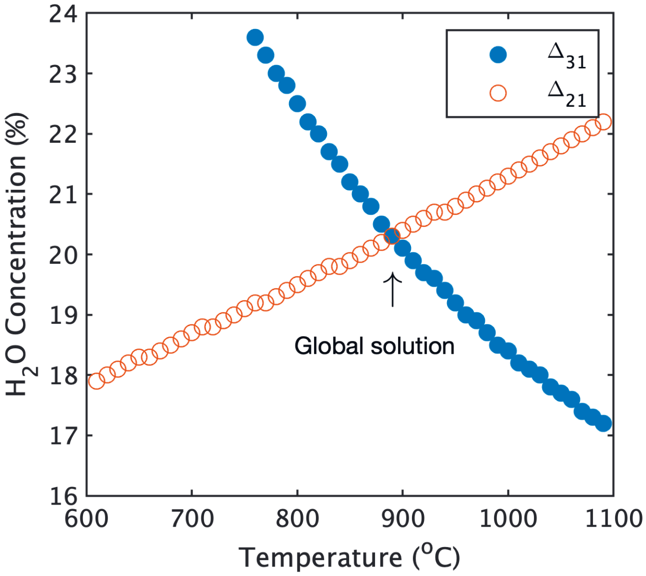

Figure 4.6 Minimum error solutions for the difference between the measured and simulated transmittance ratios Δ_{21} and Δ_{31}. **[Publication II]**

An example of the recorded signal is shown in Figure 4.5. One can observe that the measured signal comprises three distinct peaks at -10 ns, 0 ns and 60 ns time delays. Corresponding to scattering by the instrument coupling mirror, the naturally present aerosol particles and the sooth sintered back-wall, respectively. Total transmittance, of all the channels, within the furnace is calculated using the signal backscattered from the instrument and the back-wall. The corresponding average temperature and concentration of H_2O in the boiler are simultaneously extracted from Equation 3.4 and Equation 3.5 with solutions for Δ_{21} and Δ_{31} presented in Figure 4.6. The global solution lies at the point of intersection between Δ_{21} and Δ_{31}, corresponding to average temperature and concentration values of 890 °C and 20.3 %, respectively. The results are in excellent agreement with the reference readings of the boiler as shown in Table 4.1.

The industrial proof-of-concept measurement demonstrated a statistical accuracy of 50 °C and 0.8 % for temperature and molecular concentration, respectively. It is important to emphasize that the results are sufficient for industrial process monitoring. Particularly for controlling the power plant air and

Table 4.1 Comparison of SC-DIAL measured average temperature and H_2O concentration with the reference values of the boiler. **[Publication II]**

Measurement	Temperature (°C)	H_2O Concentration (%)
Reference	850	20 – 25
SC-DIAL	890	20.3

fuel feeds for optimal operational conditions, which would in turn lower NOx emissions. A brief comparison of the SC-DIAL technique with other selected solutions is presented in Table 4.2.

Table 4.2 Comparison of SC-DIAL thermometry approach reported in Publication I and II to other selected methods. Techniques are compared based on measurement time (τ), accuracy (δ) and whether it has been implemented (Implem.) in industrial measurement context. LIA: laser induced acoustic technique.

Technique	δ (°C)	τ (ms)	Implem.	Reference
SC-DIAL	50	230	Yes	**Publication I, II**
Scheimflug lidar	100	8	No	[16]
TDLS	25	2000	Yes	[83]
LIA	77	5	No	[84]

5

Spatially resolved analysis of flue gas parameters

This chapter explores the feasibility of spatially resolving the distribution of flue gas parameters in the boiler furnace, by taking advantage of the strong backscattering by the aerosol particles. Specifically, H_2O parameters in the furnace are mapped using the SC-DIAL methodology introduced in Chapter 3. Furthermore, the negligibly absorbing Ch1 backsacttered signal is utilized to map aerosol concentration distribution along the beam path using the Klett inversion method. Detailed discussion of the results of this work is presented in **Publication IV**.

5.1 Water vapor analysis in an industrial boiler

The signal backscattered by the aerosol particles, shown in Figure 4.5, is split into discrete segments of 30 cm to simultaneously map the variation of H_2O temperature and concentration along the beam path. The optical thickness of this segment is extremely small, therefore, a high signal-to-noise ratio (SNR) is central to spatially resolve variation of the flue gas parameters. For this purpose, the experimental setup is upgraded to comprise a field programmable gate array (FPGA) for continuous averaging of SC pulses at the laser repetition rate, and more sensitive photodetectors and filters with optimal bandwidth selection of the differently absorbing spectral channels. The interference filters have a FWHM of 50 nm and central wavelengths of 1275 nm, 1375 nm and 1475 nm, respectively. Despite the aforementioned optimizations, the resulting SNR of the current measurement is insufficient to spatially resolve H_2O temperature. However, the gas concentration can be resolved by assuming a known temperature, since the temperature induced relative change in transmittance within

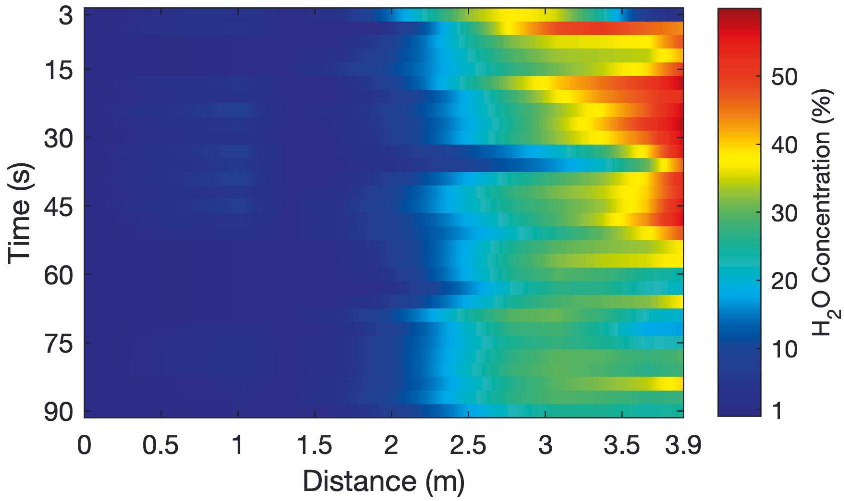

Figure 5.1 Measured real-time distribution of water vapor, along the beam path, in the power plant boiler. **[Publication IV]**

a given segment is equivalent to the amplitude of the measured signal noise. With that consideration, H_2O concentration is spatially resolved using the reference average boiler temperature value of 850 °C, across all the segments, in Equation 3.4. The resulting temporal map of H_2O concentration distribution up to 3.9 m inside the boiler, limited by the SNR, is shown in Figure 5.1.

5.2 Combustion aerosol analysis

This section extends the SC-lidar approach to measurement of combustion aerosol particle distribution, and presented its application to real-time analysis of coarse aerosol particle distribution in a power plant boiler. The results of this work are presented in **Publication IV**.

Besides aiding range-resolved measurement of temperature and molecular concentrations in the furnace, analysis of combustion aerosols itself can yield additional crucial information regarding, for instance, fuel quality [85] as well as boiler bed conditions [86] which plays a key role in terms of process optimization. Furthermore, the presence of alkali chloride particles in power plant boilers can lead to adverse effects and malfunctions. For example salt particles like KCl and CaCl can deposit on critical parts of the combustion unit like heat exchangers. And their consequent reaction with the surfaces often leads to corrosion [87–89] and fouling [90–92] which in turn can critically undermine the convective heat transfer essential for the combustion process.

Monitoring of combustion aerosols have traditionally relied on extracting the particles via a suction tube to a designated measurement instrument [93, 94]. Challenges associated with this approach including moisture, latency and possible nucleation or coagulation of the particles hinders its applicability to in-situ monitoring. In this regard, the SC-lidar presents a novel possibility for robust monitoring of combustion aerosol as demonstrated below.

As introduced in Chapter 3, the measured extinction α of a lidar signal broadly depends on absorption by gaseous molecules α_{abs} and scattering by aerosol particles α_{sca}, such that $\alpha = \alpha_{abs} + \alpha_{sca}$. The aerosol extinction is generally wavelength dependent especially in Rayleigh and Mie regime. However, considering homogeneous composition of aerosols dominated by coarse particles in the furnace and relatively narrow band of the SC-lidar spectral channels, α_{sca} is mainly proportional to the particle volume fraction on the beam path. The presented SC-lidar return is modified to include the scattering effect which yields

$$S_n(R) = \beta(R)\frac{O(R)}{R^2}\int_{\Delta\lambda_n} P_0(\lambda)\Gamma_n(\lambda)e^{-2\int_0^R \alpha_{abs}(\lambda,T,R')+\alpha_{sca}(R')\,dR'}\,d\lambda. \tag{5.1}$$

Extinction of the signal by absorption can be neglected when using a negligibly absorbing spectral channel, like Ch1 of the SC-lidar. Thereby reducing the equation above to

$$S_1(R) = \beta(R)\frac{O(R)}{R^2}P_1 e^{-2\int_0^R \alpha(R')\,dR'}, \tag{5.2}$$

where $P_1 = \int_{\Delta\lambda_n} P_0(\lambda)\Gamma_1(\lambda)\,d\lambda$. Note that for a homogeneous aerosol mixture $\beta = L\alpha$ [95], where L is a ratio of aerosol specific backscattering to extinction coefficient. Equation 5.2 is analogous to typical elastic backscatter lidar equation, thus, one can estimate the aerosol distribution in the furnace by solving

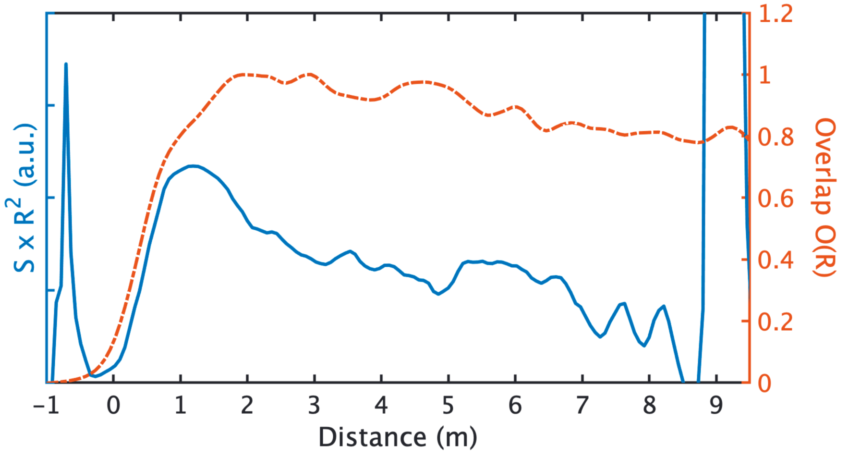

Figure 5.2 Ch1 range corrected signal (solid line) and the measured SC-lidar overlap profile (dashed line). **[Publication IV]**

for the extinction coefficient using the Klett inversion method [95, 96]. This method is commonly used in atmospheric lidar applications [97]. It estimates extinction coefficient in a reference distance using

$$\alpha(R) = \frac{e^{W(R)-W(R_m)}}{\frac{1}{\alpha(R_m)} + 2\int_R^{R_m} e^{W(R')-W(R_m)}\,dR'}, \tag{5.3}$$

where W represents logarithmic range corrected signal ($\ln[\frac{S_1(R)R^2}{O(R)}]$), R_m is a reference distance (such that $R < R_m$). The initial values of extinction at a given reference distance can also be estimated using a simple slope method suggested by Klett as $\alpha(R_m) = \frac{1}{2}\frac{W_0-W_m}{R_m-R_0}$, where the zero subscript indicates the starting point of the slope. This implies that it suffice to know the geometrical overlap function, the Ch1 aerosol backscattered signal and the measurement distance in order to estimate the extinction coefficient.

5.3 Aerosol distribution in an industrial boiler

The aerosol distribution in the furnace can be retrieved from the aerosol backscattered signal at spectral channel with negligible absorbance in the beam path, i.e. Ch1 in this case. This ensures that the extinction of the lidar beam is mainly due to scattering by the aerosol particles. The overlap factor $O(R)$

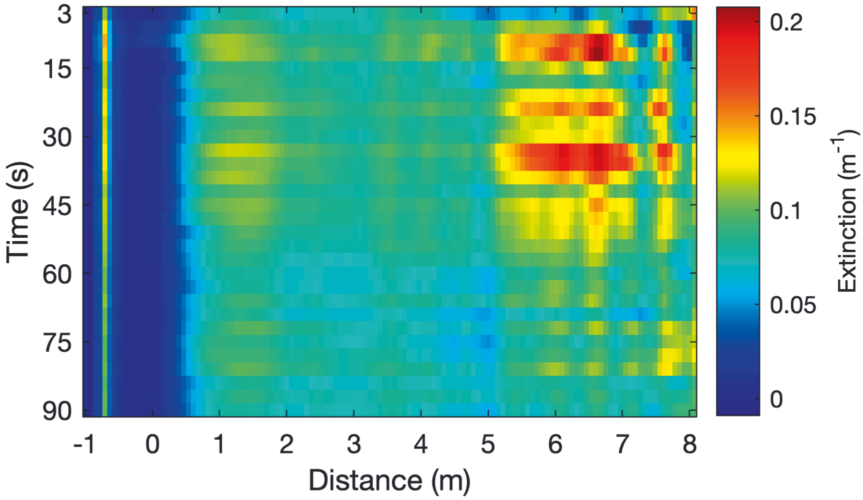

Figure 5.3 Measured real-time distribution of combustion aerosol particles in a biomass power plant boiler. **[Publication IV]**

is evaluated by continuously displacing a hard target over a given distance R and measuring the backscattered signal multiple times. The measurement was done outside of the boiler furnace to exclude aerosol extinction effect inside the boiler. The overlap factor of the SC-lidar and the measurement distance are then utilized to cancel out the geometrical effect on the signal. The resulting range corrected signal (solid blue line) and the overlap profile (dashed red line) of the SC-lidar are shown in Figure 5.2.

The interval of $1-8\,\mathrm{m}$, with a clear slope and adequate SNR, in the signal is used to calculate the initial values for extinction. Which are then used in Equation 5.3 to extract the aerosol extinction coefficient across the furnace. This yields a dynamic aerosol particle concentration distribution across the furnace, with extinction values in the range of $0.04-0.2\,\mathrm{m}^{-1}$ as shown in Figure 5.2. Our result can be used to complement flow measurements in the furnace due to the correlation between air flow and particle distribution. It also offers novel perspective for versatile real-time analysis of combustion aerosol particles.

6

Hyperspectral sensing

Recent advances in integrated photonics technologies enables miniaturized tunable filters with rapid scanning capability, which is central to the realization of robust hyperspectral remote sensing. Applications of hyperspectral sensing have since been demonstrated in various fields including mineral exploration [98], agricultural survey [99] and medical imaging [100]. Most of these conventional methods rely on passive illumination (i.e., ambient light) of the probed targets, thus, making their spectral data prone to noise and instabilities. Alternative methods employing a near infrared supercontinuum light source for active target illumination have been demonstrated [101, 102]. Active mid-infrared hyperspectral sensing, by a spectrometer employing a miniaturized Fabry-Pérot interferometer (FPI), have also been reported [103, 104]. Although the solutions proffered in these works [103, 104] are quite promising, the filter and detector are integrated as a single unit. This limits flexibility of the sensor in terms of design as well as choice of photodetector. Therefore, further study is crucial to fully realize the potential of these sensors.

This chapter explores extending the presented supercontinuum lidar towards a more generic hyperspectral sensing in the mid-infrared, using a stand-alone MEMS based FPI filter. The MEMS-FPI filter replaces the multiplex filter arrangement, while enabling rapid scanning across the broad SC spectral bandwidth and collecting more light with a more compact and simpler setup. The filter is part of MEMS-FPI solutions developed at VTT Technical Research Center of Finland Ltd [105–108]. The filter transmission band is defined by the FPI resonator air gap, separated by two highly reflective mirrors, which is voltage tunable. Hence, the transmission band of the filter can be tuned contin-

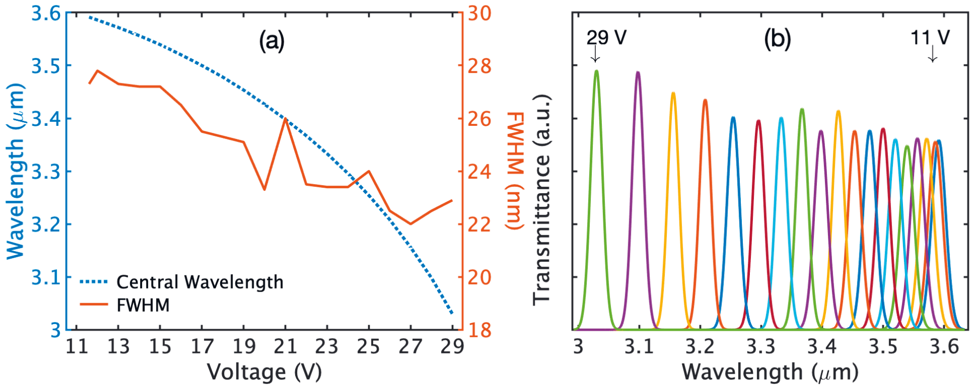

Figure 6.1 Tuning parameters of the FPI filter. (a) The corresponding central wavelength (blue dashed line) as well as the FWHM (red line) with respect to the tuning voltage. (b) Transmittance spectra of the FPI as a function of the operating voltage indicated by different colors in the figure. **[Publication III]**

uously across the spectral range of interest. Figure 6.1 presents the operational parameters of the FPI. Figure 6.1 (a) shows the resulting central wavelength and the corresponding full-width-half-maximum (FWHM) of the transmission bands as a function of the tuning voltage. Figure 6.1 (b) shows the transmittance spectrum of the FPI with respect to the corresponding operating voltage range of interest.

6.1 Stand-off hyperspectral identification of plastics

This section ascertains the hyperspectral sensing capability of the SC-lidar by experimentally demonstrating real-time remote identification of plastics. This is also the first demonstration of the suitability of the FPI towards polymer detection. The results of this work are reported in **Publication III**.

Recycling of plastic waste have been at the forefront of environmental sustainability, owing to their ever increasing pollution of the environment. Among plastic waste, black plastics tend to constitute a broader range of materials due to their various technical applications in addition to household uses. Therefore, recycling of black plastics is extremely valuable from both economic and environmental perspective. The pigment in black plastics stems from the car-

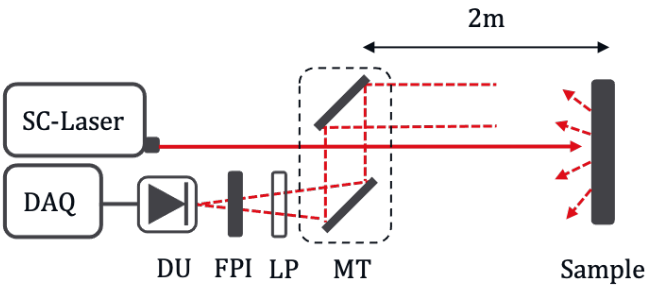

Figure 6.2 Experimental setup for stand-off hyperspectral reflectance measurement. MT: mirror telescope, LP: longpass filter, DU: detection unit, FPI: Fabry-Pérot interferometer and DAQ: data acquisition. **[Publication III]**

bon based additives, such as soot, to meet certain technical requirements [109]. Consequently making black plastics strongly absorb NIR light, which complicates their detection with conventional NIR sensors [110, 111]. Solutions based on FTIR [112–114] and LIBS [115] have been proposed, however, they are too slow for large scale sorting applications. Other technique utilizing fluorescence labeling have been demonstrated [116], however, the need for sample preparations makes it tedious for industrial applications as speed and ease of use are among the critical prerequisite.

The strong reflectance of black plastics in the MIR coupled with the strong fundamental vibrational transition of hydrogen bondings, makes MIR spectroscopy extremely attractive for robust plastic sorting. The instrument reported in **Publication III** is among the first reported MIR SC-based hyperspectral sensors [103, 104], and the first experimental demonstration of its suitability to robust plastic identification. Where it competes with established MIR hyperspectral cameras, and advanced techniques based on photon up-conversion [117] currently being researched.

The experimental arrangement for the plastic reflectance measurement, which is reproduced from **Publication III**, is shown in Figure 6.2. Detailed description of the spectrally tailored mid-infrared supercontinuum light source can be found in Ref. [118]. The reflectance spectrum of a sample can be determined by

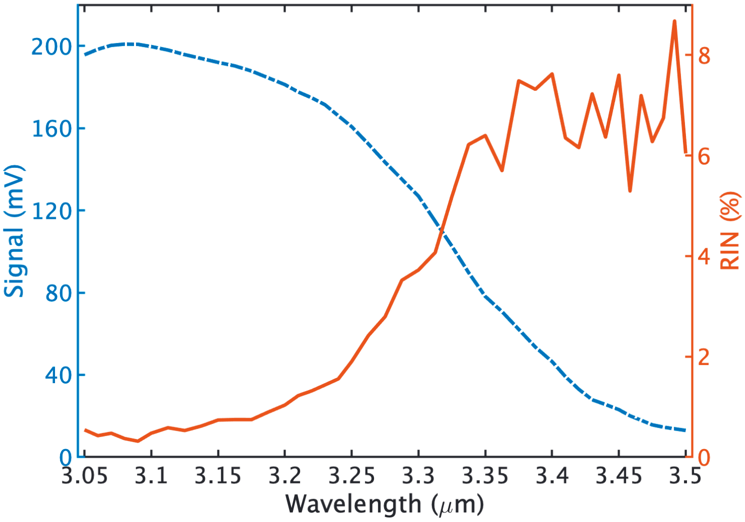

Figure 6.3 Measured backscattered intensity spectrum from a diffuser (dashed blue line) and the corresponding relative intensity noise of the measurement (thick red line). **[Publication III]**

$$r = \frac{I_S - N_B}{I_R - N_B}, \tag{6.1}$$

where I_R and I_S are the measured spectrum of the reference target and the sample, respectively, N_B is the background noise. Figure 6.3 presents an example of the measured backscattered intensity spectrum from a diffuser (i.e. the reference target), and the corresponding relative intensity noise (RIN) calculated based on 10 consecutive measurements. Note that the resulted spectral shape is representative of the SC spectrum, as both the diffuser reflectance and the detector responsivity are flat at this wavelength range.

Black polypropylene (PP) and polyethylene (PE500) are selected as the main black plastic samples of interest, as they are among the primary black plastic waste particularly among waste electrical and electronic equipment (WEEE) [108]. They are also difficult to distinguish owing to the extreme similarity in their spectral absorption features. The reflectance spectra of the plastics are successfully measured. They are then compared to their reference FTIR spectra, as shown in Figure 6.4, in order to ascertain the reliability of the measurements.

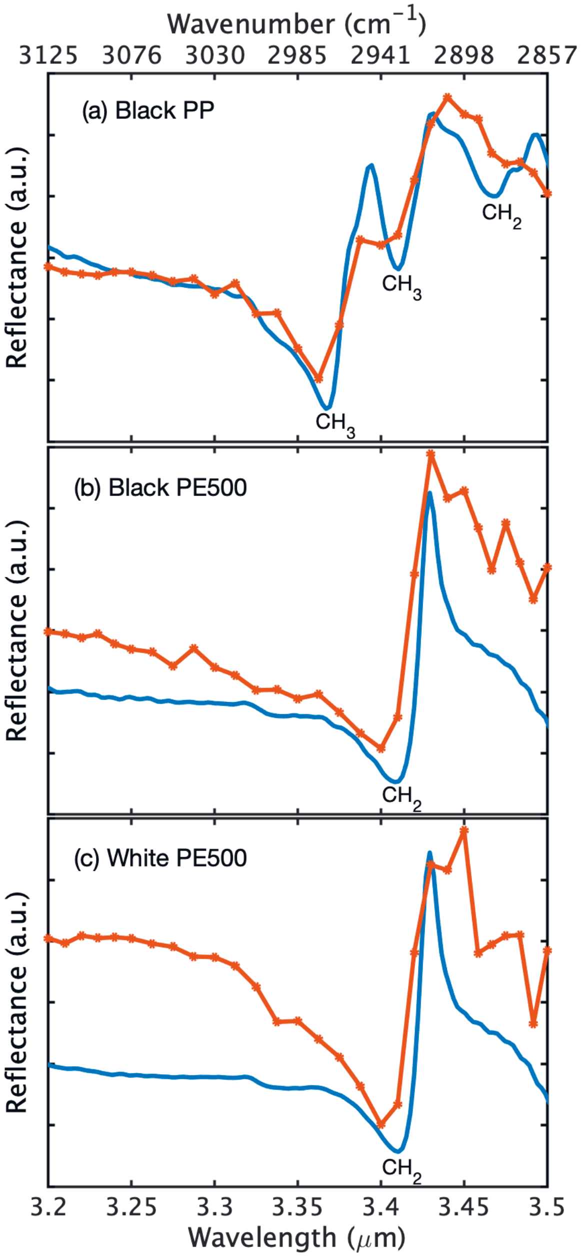

Figure 6.4 Measured reflectance spectra (red line with a marker) of plastics compared to their reference FTIR spectra (blue line). **[Publication III]**

The resulting reflectance spectra are in excellent agreement to their FTIR reference, and the plastics are clearly distinguishable. The reflectance spectra of a white PE500 is also measured, and it shows negligible difference in comparison to its black counterpart. This highlights the negligible effect of the coloring material on the optical properties of the plastics at this wavelength range. Thus, emphasizing the applicability of the sensor to differently colored plastics.

6.2 Future prospects of hyperspectral SC-lidar

Although promising results have so far been achieved by the hyperspectral SC-lidar, further optimization in terms of SNR and miniaturization is central to fully realize the commercial potential of this technology. This can be achieved by employing advanced IR photonics and MEMS technologies. For example, the pump laser could be replaced with a microchip laser or a high-peak-power multimode fiber laser [119, 120]. The impact of the multimode fiber laser beam quality is negligible since the detection range is relatively short. Moreover, recent research results have also shown spatial beam self cleaning by supercontinuum generation in multimode fiber lasers [121–125], which further enhances the beam quality. Further optimization of the scanning rate of the introduced MEMS-FPI filter, by tailoring the temporal scanning profile to have longer integration time for the noisy part of the spectrum would significantly enhance the SNR.

Finally, MEMS beam steering technologies currently under development for various consumer devices, most notably in automotive lidars and head mounted displays among others, would enable robust 3D point cloud scanning. These improvements along with others, would allow the supercontinuum lidar to fully demonstrate robust real-time 3D hyperspectral remote sensing for versatile short range industrial applications. While also paving the way for other long range applications.

7

Summary and outlook

Optical remote sensing techniques are essential to analyze distant targets, enabling nonintrusive quantification or identification of substances as well as monitoring of evolutive phenomena underlining dynamical physical processes. Various techniques like light detection and ranging (lidar) are well established and even commercially available for various applications. With the ever-increasing demand for exploitation of broadband light sources with novel spectral windows for robust and simultaneous multi-spectral analysis, lidar techniques continue to be the subject of intense research efforts. Particularly in the field of combustion diagnostics, where nonintrusive remote monitoring of localized flue gas parameters is central to the optimization of the process performance. Besides, this research is also of great interest to other short range industrial applications. This thesis presents novel and original contributions to the overall development of a broadband lidar system. The various concepts developed in this work are demonstrated and experimentally validated, which sets the framework for future technologies.

The thesis began with the development of a novel broadband supercontinuum lidar system and the first demonstration of the technique to large scale combustion thermometry. This type of data is of primary importance for biomass powered combustion units, due to the inhomogeneous nature of the fuel. Precise control, of for example fuel and oxygen feed, and management of the combustion process demands localized real-time measurements. Enabling increased energy production efficiency while decreasing the emission of harmful pollutants. Various alternative methods have been demonstrated for this purpose, yielding various results. Proof-of-concept demonstration by the supercontinuum lidar demonstrated a temperature measurement accuracy of about 40 °C in a laboratory setting, which is far superior to the reported values with other proposed lidar solutions [15–18].

After the laboratory scale proof-of-concept demonstration, the supercontinuum lidar is extended to real-time measurement of flue gas parameters in a full-scale industrial boiler. Average parameters of water vapor temperature and concentration are measured with a statistical accuracy of 50 °C and 0.8 %, respectively. The achieved accuracy is sufficient for industrial process analysis, especially for fuel and air feeds which are essential for low NOx emissions. Taking advantage of the combustion aerosol backscattering, variation of water vapor concentration in the boiler is also spatially resolved up to about 4 m into the boiler. Further, combustion aerosol distribution in the boiler is mapped using the Klett inversion method, yielding extinction values of $0.04 - 0.2\,\mathrm{m}^{-1}$. The results of this work offers novel perspective for versatile real-time monitoring of flue gas parameters and other industrial process analysis.

The final part of the thesis explores extending the supercontinuum lidar towards a more generic hyperspectral sensing in the mid-infrared spectral range, to take advantage of the so called molecular finger print region where molecules demonstrate strong and characteristic absorption features. The multiplex filters of the SC-lidar are replaced with a MEMS-based filter, enabling continuous on axis filtering of the supercontinuum spectral components, thus, yielding more spectral data. Hyperspectral measurement capability of the SC-lidar is evaluated by identification of black plastics. This is of great interest as black plastics detection with conventional sensors is rather complicated by their strong absorption in the near infrared. The SC-lidar measured reflectance spectra of the plastics are in excellent agreement with their reference FTIR spectra. A white colored plastic reflectance spectra is also measured to highlight the potential applicability of the sensor to differently colored plastics. The results demonstrate a unique potential in comparison to other methods like mid-infrared hyperspectral cameras, which have seen implementation, and other advanced techniques based on photon up-conversion [117] which are rather complex to implement in industrial measurement context. Finally, the SC-lidar technology is currently being further developed for enhanced sensitivity and miniaturization, with an ultimate goal of real time 3D point cloud mapping and analysis in industrial environments.

REFERENCES

[1] A. Behrendt. *Temperature measurements with lidar*. Springer, 2005.

[2] Y. F. Arshinov, S. M. Bobrovnikov, V. E. Zuev and V. Mitev. "Atmospheric temperature measurements using a pure rotational Raman lidar". *Applied Optics* 22.19 (1983), pp. 2984–2990.

[3] J. B. Mason. "Lidar measurement of temperature: a new approach". *Applied optics* 14.1 (1975), pp. 76–78.

[4] E. Simley, L. Pao, R. Frehlich, B. Jonkman and N. Kelley. "Analysis of wind speed measurements using continuous wave LIDAR for wind turbine control". In: *49th AIAA Aerospace Sciences Meeting including the New Horizons Forum and Aerospace Exposition.* 2011, p. 263.

[5] W. B. Grant. "Differential absorption and Raman lidar for water vapor profile measurements: a review". *Optical Engineering* 30.1 (1991), pp. 40–48.

[6] A. Ben-David. "Backscattering measurements of atmospheric aerosols at CO_2 laser wavelengths: implications of aerosol spectral structure on differential-absorption lidar retrievals of molecular species". *Applied optics* 38.12 (1999), pp. 2616–2624.

[7] R. A. Haugerud, D. J. Harding, S. Y. Johnson, J. L. Harless, C. S. Weaver and B. L. Sherrod. "High-resolution lidar topography of the Puget Lowland, Washington". *GSA Today* 13.6 (2003), pp. 4–10.

[8] T. Kabel, C. T. Georgakis and A. R. Zeeberg. "Mapping ocean waves using new lidar equipment". In: *The 29th International Ocean and Polar Engineering Conference.* OnePetro. 2019.

[9] S. Svanberg. "Fluorescence lidar monitoring of vegetation status". *Physica Scripta* 1995.T58 (1995), p. 79.

[10] J. Xian, D. Sun, W. Xu, Y. Han, J. Zheng, J. Peng and S. Yang. “Urban air pollution monitoring using scanning Lidar”. *Environmental Pollution* 258 (2020), p. 113696.

[11] L. Pantani, G. Ballerini, G. Cecchi, H. Edner, D. Lognoli, T. Johansson, V. Raimondi, S. Svanberg, P. Tiano, L. Tomaselli et al. “Experiments on stony monument monitoring by laser-induced fluorescence”. *Journal of Cultural Heritage* 1 (2000), S345–S348.

[12] N. Borowiec and U. Marmol. “Using LiDAR System as a Data Source for Agricultural Land Boundaries”. *Remote Sensing* 14.4 (2022), p. 1048.

[13] P. McKendry. “Energy production from biomass (part 1): overview of biomass”. *Bioresource technology* 83.1 (2002), pp. 37–46.

[14] M. Hupa, O. Karlström and E. Vainio. “Biomass combustion technology development–It is all about chemical details”. *Proceedings of the Combustion institute* 36.1 (2017), pp. 113–134.

[15] E. Malmqvist, M. Brydegaard, M. Aldén and J. Bood. “Scheimpflug lidar for combustion diagnostics”. *Optics express* 26.12 (2018), pp. 14842–14858.

[16] E. Malmqvist, J. Borggren, M. Aldén and J. Bood. “Lidar thermometry using two-line atomic fluorescence”. *Applied optics* 58.4 (2019), pp. 1128–1133.

[17] B. Kaldvee, A. Ehn, J. Bood and M. Aldén. “Development of a picosecond lidar system for large-scale combustion diagnostics”. *Applied optics* 48.4 (2009), B65–B72.

[18] B. Kaldvee, J. Bood and M. Aldén. “Picosecond-lidar thermometry in a measurement volume surrounded by highly scattering media”. *Measurement Science and Technology* 22.12 (2011), p. 125302.

[19] R. R. Alfano. *The supercontinuum laser source: fundamentals with updated references*. Springer, 2006.

[20] J. M. Dudley and J. R. Taylor. *Supercontinuum generation in optical fibers*. Cambridge University Press, 2010.

[21] I. Newton. “A letter of Mr. Isaac Newton, Professor of the Mathematicks in the University of Cambridge; containing his new theory about light and colors: sent by the author to the publisher from Cambridge, Febr. 6. 1671/72; in order to be communicated to the R. Society”. *Philosophical Transactions of the Royal Society of London* 6.80 (1672), pp. 3075–3087. DOI: 10.1098/rstl.1671.0072.

[22] K. Fuwa and B. Valle. “The Physical Basis of Analytical Atomic Absorption Spectrometry. The Pertinence of the Beer-Lambert Law.” *Analytical Chemistry* 35.8 (1963), pp. 942–946.

[23] G. Grynberg, A. Aspect and C. Fabre. *Introduction to quantum optics: from the semi-classical approach to quantized light.* Cambridge university press, 2010.

[24] J. M. Hollas. *Modern spectroscopy.* John Wiley & Sons, 2004.

[25] L. S. Rothman, I. E. Gordon, Y. Babikov, A. Barbe, D. C. Benner, P. F. Bernath, M. Birk, L. Bizzocchi, V. Boudon, L. R. Brown et al. “The HITRAN2012 molecular spectroscopic database”. *Journal of Quantitative Spectroscopy and Radiative Transfer* 130 (2013), pp. 4–50.

[26] P. M. Chu, F. R. Guenther, G. C. Rhoderick and W. J. Lafferty. “The NIST quantitative infrared database”. *Journal of research of the National Institute of Standards and Technology* 104.1 (1999), p. 59.

[27] L. Brown, M. Gunson, R. Toth, F. Irion, C. Rinsland and A. Goldman. “1995 atmospheric trace molecule spectroscopy (ATMOS) linelist”. *Applied Optics* 35.16 (1996), pp. 2828–2848.

[28] S. W. Sharpe, T. J. Johnson, R. L. Sams, P. M. Chu, G. C. Rhoderick and P. A. Johnson. “Gas-phase databases for quantitative infrared spectroscopy”. *Applied spectroscopy* 58.12 (2004), pp. 1452–1461.

[29] N. Jacquinet-Husson, E. Arie, J. Ballard, A. Barbe, G. Bjoraker, B. Bonnet, L. Brown, C. Camy-Peyret, J. Champion, A. Chedin et al. “The 1997 spectroscopic GEISA databank”. *Journal of Quantitative Spectroscopy and Radiative Transfer* 62.2 (1999), pp. 205–254.

[30] L. S. Rothman, I. Gordon, R. Barber, H. Dothe, R. R. Gamache, A. Goldman, V. Perevalov, S. Tashkun and J. Tennyson. "HITEMP, the high-temperature molecular spectroscopic database". *Journal of Quantitative Spectroscopy and Radiative Transfer* 111.15 (2010), pp. 2139–2150.

[31] C. Weitkamp. *Lidar: range-resolved optical remote sensing of the atmosphere.* Vol. 102. Springer Science & Business, 2006.

[32] P. Dong and Q. Chen. *LiDAR remote sensing and applications.* CRC Press, 2017.

[33] Z. Liu, A. Omar, M. Vaughan, J. Hair, C. Kittaka, Y. Hu, K. Powell, C. Trepte, D. Winker, C. Hostetler et al. "CALIPSO lidar observations of the optical properties of Saharan dust: A case study of long-range transport". *Journal of Geophysical Research: Atmospheres* 113.D7 (2008).

[34] C. Marchant, T. D. Wilkerson, G. E. Bingham, V. V. Zavyalov, J. M. Andersen, C. Wright, S. S. Cornelsen, R. S. Martin, P. J. Silva and J. L. Hatfield. "Aglite lidar: a portable elastic lidar system for investigating aerosol and wind motions at or around agricultural production facilities". *Journal of Applied Remote Sensing* 3.1 (2009), p. 033511.

[35] C. Fruck, M. Gaug, A. Hahn, V. Acciari, J. Besenrieder, D. Dominis Prester, D. Dorner, D. Fink, L. Font, S. Mićanović et al. "Characterizing the aerosol atmosphere above the Observatorio del Roque de los Muchachos by analysing seven years of data taken with an GaAsP HPD-readout, absolutely calibrated elastic LIDAR". *Monthly Notices of the Royal Astronomical Society* 515.3 (2022), pp. 4520–4550.

[36] P. Dellenbach, J.-E. Deschaud, B. Jacquet and F. Goulette. "CT-ICP: Real-time elastic LiDAR odometry with loop closure". In: *2022 International Conference on Robotics and Automation (ICRA).* IEEE. 2022, pp. 5580–5586.

[37] O. Reitebuch, C. Werner, I. Leike, P. Delville, P. H. Flamant, A. Cress and D. Engelbart. "Experimental validation of wind profiling performed by the airborne 10-μm heterodyne Doppler lidar WIND". *Journal of Atmospheric and Oceanic Technology* 18.8 (2001), pp. 1331–1344.

[38] G. Benedetti-Michelangeli, F. Congeduti and G. Fiocco. "Measurement of aerosol motion and wind velocity in the lower troposphere by Doppler optical radar". *Journal of Atmospheric Sciences* 29.5 (1972), pp. 906–910.

[39] C. Werner. *Doppler wind lidar*. Springer, 2005.

[40] G. Vaughan, D. Wareing, S. Pepler, L. Thomas and V. Mitev. "Atmospheric temperature measurements made by rotational Raman scattering". *Applied optics* 32.15 (1993), pp. 2758–2764.

[41] A. Behrendt and J. Reichardt. "Atmospheric temperature profiling in the presence of clouds with a pure rotational Raman lidar by use of an interference-filter-based polychromator". *Applied Optics* 39.9 (2000), pp. 1372–1378.

[42] D. H. Kim, H. K. Cha, J. M. Lee and S. Bobronikov. "Pure rotational Raman lidar for atmospheric temperature measurements". *Journal of the Korean Physical Society* 39 (2001).

[43] U. Wandinger. *Raman lidar*. Springer, 2005.

[44] L. Palombi, D. Alderighi, G. Cecchi, V. Raimondi, G. Toci and D. Lognoli. "A fluorescence LIDAR sensor for hyper-spectral time-resolved remote sensing and mapping". *Optics Express* 21.12 (2013), pp. 14736–14746.

[45] C. W. Wright, F. E. Hoge, R. N. Swift, J. K. Yungel and C. R. Schirtzinger. "Next-generation NASA airborne oceanographic lidar system". *Applied optics* 40.3 (2001), pp. 336–342.

[46] P. Weibring, H. Edner and S. Svanberg. "Versatile mobile lidar system for environmental monitoring". *Applied Optics* 42.18 (2003), pp. 3583–3594.

[47] L. Mei and M. Brydegaard. "Continuous-wave differential absorption lidar". *Laser & Photonics Reviews* 9.6 (2015), pp. 629–636.

[48] E. V. Browell, T. D. Wilkerson and T. J. McIlrath. "Water vapor differential absorption lidar development and evaluation". *Applied optics* 18.20 (1979), pp. 3474–3483.

[49] E. Browell, S. Ismail and W. Grant. "Differential absorption lidar (DIAL) measurements from air and space". *Applied Physics B* 67 (1998), pp. 399–410.

[50] G. J. Koch, B. W. Barnes, M. Petros, J. Y. Beyon, F. Amzajerdian, J. Yu, R. E. Davis, S. Ismail, S. Vay, M. J. Kavaya et al. “Coherent differential absorption lidar measurements of CO_2”. *Applied optics* 43.26 (2004), pp. 5092–5099.

[51] F. Innocenti, R. Robinson, T. Gardiner, A. Finlayson and A. Connor. “Differential absorption lidar (DIAL) measurements of landfill methane emissions”. *Remote sensing* 9.9 (2017), p. 953.

[52] R. Alfano and S. Shapiro. “Emission in the region 4000 to 7000 Å via four-photon coupling in glass”. *Physical Review Letters* 24.11 (1970), p. 584.

[53] J. I. Gersten, R. Alfano and M. Belic. “Combined stimulated Raman scattering and continuum self-phase modulations”. *Physical review A* 21.4 (1980), p. 1222.

[54] J. Knight, T. Birks, P. S. J. Russell and D. Atkin. “All-silica single-mode optical fiber with photonic crystal cladding”. *Optics letters* 21.19 (1996), pp. 1547–1549.

[55] A. D. Aguirre, N. Nishizawa, J. G. Fujimoto, W. Seitz, M. Lederer and D. Kopf. “Continuum generation in a novel photonic crystal fiber for ultrahigh resolution optical coherence tomography at 800 nm and 1300 nm”. *Optics Express* 14.3 (2006), pp. 1145–1160.

[56] T. A. Birks, J. C. Knight and P. S. J. Russell. “Endlessly single-mode photonic crystal fiber”. *Optics letters* 22.13 (1997), pp. 961–963.

[57] K. Saitoh and M. Koshiba. “Empirical relations for simple design of photonic crystal fibers”. *Optics express* 13.1 (2005), pp. 267–274.

[58] J. K. Ranka, R. S. Windeler and A. J. Stentz. “Visible continuum generation in air–silica microstructure optical fibers with anomalous dispersion at 800 nm”. *Optics letters* 25.1 (2000), pp. 25–27.

[59] S. Coen, A. H. L. Chau, R. Leonhardt, J. D. Harvey, J. C. Knight, W. J. Wadsworth and P. S. J. Russell. “Supercontinuum generation by stimulated Raman scattering and parametric four-wave mixing in photonic crystal fibers”. *JOSA B* 19.4 (2002), pp. 753–764.

[60] C. Xia, M. Kumar, O. P. Kulkarni, M. N. Islam, F. L. Terry Jr, M. J. Freeman, M. Poulain and G. Mazé. “Mid-infrared supercontinuum generation to 4.5 μm in ZBLAN fluoride fibers by nanosecond diode pumping”. *Optics letters* 31.17 (2006), pp. 2553–2555.

[61] J. M. Dudley, G. Genty and S. Coen. “Supercontinuum generation in photonic crystal fiber”. *Reviews of modern physics* 78.4 (2006), p. 1135.

[62] Y. Chen, E. Räikkönen, S. Kaasalainen, J. Suomalainen, T. Hakala, J. Hyyppä and R. Chen. “Two-channel hyperspectral LiDAR with a supercontinuum laser source”. *Sensors* 10.7 (2010), pp. 7057–7066.

[63] G. Méjean, J. Kasparian, E. Salmon, J. Yu, J.-P. Wolf, R. Bourayou, R. Sauerbrey, M. Rodriguez, L. Wöste, H. Lehmann et al. “Towards a supercontinuum-based infrared lidar”. *Applied Physics B* 77 (2003), pp. 357–359.

[64] S. Kaasalainen, T. Lindroos and J. Hyyppa. “Toward hyperspectral lidar: Measurement of spectral backscatter intensity with a supercontinuum laser source”. *IEEE Geoscience and Remote Sensing Letters* 4.2 (2007), pp. 211–215.

[65] D. Bradley and K. Matthews. “Measurement of high gas temperatures with fine wire thermocouples”. *Journal of mechanical engineering science* 10.4 (1968), pp. 299–305.

[66] E. Vainio, A. Brink, M. Hupa, H. Vesala and T. Kajolinna. “Fate of fuel nitrogen in the furnace of an industrial bubbling fluidized bed boiler during combustion of biomass fuel mixtures”. *Energy & fuels* 26.1 (2012), pp. 94–101.

[67] E. Vainio. “Fate of fuel-bound nitrogen and sulfur in biomass-fired Industrial boilers” (2014).

[68] A. Farooq, J. B. Jeffries and R. K. Hanson. “In situ combustion measurements of H2O and temperature near 2.5 μm using tunable diode laser absorption”. *Measurement Science and Technology* 19.7 (2008), p. 075604.

[69] J. Liu, J. Jeffries and R. Hanson. “Wavelength modulation absorption spectroscopy with 2 f detection using multiplexed diode lasers for rapid

temperature measurements in gaseous flows”. *Applied Physics B* 78 (2004), pp. 503–511.

[70] X. Zhou, J. Jeffries and R. Hanson. “Development of a fast temperature sensor for combustion gases using a single tunable diode laser”. *Applied Physics B* 81 (2005), pp. 711–722.

[71] G. B. Rieker, J. B. Jeffries and R. K. Hanson. “Calibration-free wavelength-modulation spectroscopy for measurements of gas temperature and concentration in harsh environments”. *Applied optics* 48.29 (2009), pp. 5546–5560.

[72] C. S. Goldenstein, R. M. Spearrin, J. B. Jeffries and R. K. Hanson. “Infrared laser-absorption sensing for combustion gases”. *Progress in Energy and Combustion Science* 60 (2017), pp. 132–176.

[73] H. Y. Zhang, K. B. Xu, F. Q. Xie and Y. Liu. “Temperature field reconstruction system based on ultrasonic time-of-flight technique”. In: *Applied Mechanics and Materials*. Vol. 271. Trans Tech Publ. 2013, pp. 1675–1679.

[74] Q. Zhong, Y. Chen, B. Zhu, S. Liao and K. Shi. “A temperature field reconstruction method based on acoustic thermometry”. *Measurement* 200 (2022), p. 111642.

[75] J. M. Seitzman, G. Kychakoff and R. K. Hanson. “Instantaneous temperature field measurements using planar laser-induced fluorescence”. *Optics letters* 10.9 (1985), pp. 439–441.

[76] A. Omrane, P. Petersson, M. Aldén and M. Linne. “Simultaneous 2D flow velocity and gas temperature measurements using thermographic phosphors”. *Applied Physics B* 92 (2008), pp. 99–102.

[77] P. Nooren, M. Versluis, T. H. van der Meer, R. Barlow and J. Frank. “Raman-Rayleigh-LIF measurements of temperature and species concentrations in the Delft piloted turbulent jet diffusion flame”. *Applied Physics B* 71 (2000), pp. 95–111.

[78] Z. Qu, R. Ghorbani, D. Valiev and F. M. Schmidt. “Calibration-free scanned wavelength modulation spectroscopy–application to H 2 O and temperature sensing in flames”. *Optics express* 23.12 (2015), pp. 16492–16499.

[79] T. Sorvajärvi, N. DeMartini, J. Rossi and J. Toivonen. “In situ measurement technique for simultaneous detection of K, KCl, and KOH vapors released during combustion of solid biomass fuel in a single particle reactor”. *Applied spectroscopy* 68.2 (2014), pp. 179–184.

[80] J. Viljanen, T. Sorvajärvi and J. Toivonen. “In situ laser measurement of oxygen concentration and flue gas temperature utilizing chemical reaction kinetics”. *Optics letters* 42.23 (2017), pp. 4925–4928.

[81] M. Aldén, A. Omrane, M. Richter and G. Särner. “Thermographic phosphors for thermometry: a survey of combustion applications”. *Progress in energy and combustion science* 37.4 (2011), pp. 422–461.

[82] J. Borggren, W. Weng, A. Hosseinnia, P.-E. Bengtsson, M. Aldén and Z. Li. “Diode laser-based thermometry using two-line atomic fluorescence of indium and gallium”. *Applied Physics B* 123 (2017), pp. 1–10.

[83] Z. Qu, P. Holmgren, N. Skoglund, D. R. Wagner, M. Broström and F. M. Schmidt. “Distribution of temperature, H2O and atomic potassium during entrained flow biomass combustion–Coupling in situ TDLAS with modeling approaches and ash chemistry”. *Combustion and Flame* 188 (2018), pp. 488–497.

[84] J. Lee, C. Bong, H. Sun, J. Jeong and M. S. Bak. “Thermometry of combustion gases using light emission and acoustic wave from laser-induced sparks”. *Journal of Physics D: Applied Physics* 52.31 (2019), p. 315201.

[85] A. Garcia-Maraver, M. Zamorano, U. Fernandes, M. Rabaçal and M. Costa. “Relationship between fuel quality and gaseous and particulate matter emissions in a domestic pellet-fired boiler”. *Fuel* 119 (2014), pp. 141–152.

[86] B.-Å. Andersson. “Effects of bed particle size on heat transfer in circulating fluidized bed boilers”. *Powder Technology* 87.3 (1996), pp. 239–248.

[87] H. P. Nielsen, F. Frandsen, K. Dam-Johansen and L. Baxter. “The implications of chlorine-associated corrosion on the operation of biomass-fired boilers”. *Progress in energy and combustion science* 26.3 (2000), pp. 283–298.

[88] E. Vainio, N. DeMartini, L. Hupa, L.-E. Åmand, T. Richards and M. Hupa. “Hygroscopic properties of calcium chloride and its role on cold-end corrosion in biomass combustion”. *Energy & Fuels* 33.11 (2019), pp. 11913–11922.

[89] R. A. Antunes and M. C. L. de Oliveira. “Corrosion in biomass combustion: A materials selection analysis and its interaction with corrosion mechanisms and mitigation strategies”. *Corrosion Science* 76 (2013), pp. 6–26.

[90] A. F. Stam, K. Haasnoot and G. Brem. “Superheater fouling in a BFB boiler firing wood-based fuel blends”. *Fuel* 135 (2014), pp. 322–331.

[91] B.-J. Skrifvars, P. Yrjas, T. Laurén, J. Kinni, H. Tran and M. Hupa. “The fouling behavior of rice husk ash in fluidized-bed combustion. 2. Pilot-scale and full-scale measurements”. *Energy & fuels* 19.4 (2005), pp. 1512–1519.

[92] M. Theis, B.-J. Skrifvars, M. Hupa and H. Tran. “Fouling tendency of ash resulting from burning mixtures of biofuels. Part 1: Deposition rates”. *Fuel* 85.7-8 (2006), pp. 1125–1130.

[93] H. Kuuluvainen, P. Karjalainen, C. J. Bajamundi, J. Maunula, P. Vainikka, J. Roppo, J. Keskinen and T. Rönkkö. “Physical properties of aerosol particles measured from a bubbling fluidized bed boiler”. *Fuel* 139 (2015), pp. 144–153.

[94] E. Gustafsson, L. Lin, M. C. Seemann, J. Rodin and M. Strand. “Characterization of particulate matter in the hot product gas from indirect steam bubbling fluidized bed gasification of wood pellets”. *Energy & Fuels* 25.4 (2011), pp. 1781–1789.

[95] J. D. Klett. “Lidar inversion with variable backscatter/extinction ratios”. en. *Applied Optics* 24.11 (June 1985), p. 1638. ISSN: 0003-6935, 1539-4522. DOI: 10.1364/AO.24.001638. URL: https://www.osapublishing.org/abstract.cfm?URI=ao-24-11-1638 (visited on 02/16/2021).

[96] J. D. Klett. “Stable analytical inversion solution for processing lidar returns”. en. *Applied Optics* 20.2 (Jan. 1981), p. 211. ISSN: 0003-6935, 1539-4522. DOI: 10.1364/AO.20.000211. URL: https://opg.optica.org/abstract.cfm?URI=ao-20-2-211 (visited on 08/11/2022).

[97] A. Comerón, C. Muñoz-Porcar, F. Rocadenbosch, A. Rodrıguez-Gómez and M. Sicard. "Current Research in Lidar Technology Used for the Remote Sensing of Atmospheric Aerosols". en. *Sensors* 17.6 (June 2017), p. 1450. ISSN: 1424-8220. DOI: 10.3390/s17061450. URL: http://www.mdpi.com/1424-8220/17/6/1450 (visited on 01/12/2023).

[98] D. Krupnik and S. Khan. "Close-range, ground-based hyperspectral imaging for mining applications at various scales: Review and case studies". *Earth-science reviews* 198 (2019), p. 102952.

[99] T. Adão, J. Hruška, L. Pádua, J. Bessa, E. Peres, R. Morais and J. J. Sousa. "Hyperspectral imaging: A review on UAV-based sensors, data processing and applications for agriculture and forestry". *Remote sensing* 9.11 (2017), p. 1110.

[100] G. Lu and B. Fei. "Medical hyperspectral imaging: a review". *Journal of biomedical optics* 19.1 (2014), pp. 010901–010901.

[101] T. Kääriäinen, P. Jaanson, A. Vaigu, R. Mannila and A. Manninen. "Active hyperspectral sensor based on MEMS Fabry-Pérot interferometer". *Sensors* 19.9 (2019), p. 2192.

[102] T. Kääriäinen and T. Dönsberg. "Active hyperspectral imager using a tunable supercontinuum light source based on a MEMS Fabry–Perot interferometer". *Optics Letters* 46.22 (2021), pp. 5533–5536.

[103] J. Kilgus, K. Duswald, G. Langer and M. Brandstetter. "Mid-infrared standoff spectroscopy using a supercontinuum laser with compact Fabry–Pérot filter spectrometers". *Applied spectroscopy* 72.4 (2018), pp. 634–642.

[104] J. Kilgus, P. Müller, P. M. Moselund and M. Brandstetter. "Application of supercontinuum radiation for mid-infrared spectroscopy". In: *Optical Sensing and Detection IV*. Vol. 9899. SPIE. 2016, pp. 117–126.

[105] A. Rissanen, A. Akujärvi, J. Antila, M. Blomberg and H. Saari. "MOEMS miniature spectrometers using tuneable Fabry-Perot interferometers". *Journal of Micro/Nanolithography, MEMS, and MOEMS* 11.2 (2012), pp. 023003–023003.

[106] A. Rissanen, R. Mannila, M. Tuohiniemi, A. Akujärvi and J. Antila. “Tunable MOEMS Fabry-Perot interferometer for miniaturized spectral sensing in near-infrared”. In: *MOEMS and Miniaturized Systems XIII*. Vol. 8977. SPIE. 2014, pp. 243–250.

[107] A. Rissanen, B. Guo, H. Saari, A. Näsilä, R. Mannila, A. Akujärvi and H. Ojanen. “VTT’s Fabry-Perot interferometer technologies for hyperspectral imaging and mobile sensing applications”. In: *Moems and Miniaturized Systems Xvi*. Vol. 10116. SPIE. 2017, pp. 119–130.

[108] C. Signoret, A.-S. Caro-Bretelle, J.-M. Lopez-Cuesta, P. Ienny and D. Perrin. “MIR spectral characterization of plastic to enable discrimination in an industrial recycling context: I. Specific case of styrenic polymers”. *Waste management* 95 (2019), pp. 513–525.

[109] A. Turner. “Black plastics: Linear and circular economies, hazardous additives and marine pollution”. *Environment international* 117 (2018), pp. 308–318.

[110] S. Serranti, A. Gargiulo and G. Bonifazi. “Characterization of post-consumer polyolefin wastes by hyperspectral imaging for quality control in recycling processes”. *Waste Management* 31.11 (2011), pp. 2217–2227.

[111] J. Beigbeder, D. Perrin, J.-F. Mascaro and J.-M. Lopez-Cuesta. “Study of the physico-chemical properties of recycled polymers from waste electrical and electronic equipment (WEEE) sorted by high resolution near infrared devices”. *Resources, Conservation and Recycling* 78 (2013), pp. 105–114.

[112] W. Hart, P. Painter, J. Koenig and M. Coleman. “A fourier transform infrared method of studying elastomers filled with carbon black”. *Applied Spectroscopy* 31.3 (1977), pp. 220–224.

[113] E. F. Devlin. “The fourier transform infrared spectrum of cured, black-reinforced SBR”. *Journal of Polymer Science: Polymer Letters Edition* 19.4 (1981), pp. 189–192.

[114] J. M. Chalmers, M. W. Mackenzie and N. Poole. “Some observations on FTIR emission spectroscopy of black solid samples”. *Microchimica Acta* 95 (1988), pp. 249–253.

[115] S.-B. Roh, S.-B. Park, S.-K. Oh, E.-K. Park and W. Z. Choi. "Development of intelligent sorting system realized with the aid of laser-induced breakdown spectroscopy and hybrid preprocessing algorithm-based radial basis function neural networks for recycling black plastic wastes". *Journal of Material Cycles and Waste Management* 20 (2018), pp. 1934–1949.

[116] S. Brunner, P. Fomin and C. Kargel. "Automated sorting of polymer flakes: Fluorescence labeling and development of a measurement system prototype". *Waste Management* 38 (2015), pp. 49–60.

[117] W. Becker, K. Sachsenheimer and M. Klemenz. "Detection of black plastics in the middle infrared spectrum (MIR) using photon up-conversion technique for polymer recycling purposes". *Polymers* 9.9 (2017), p. 435.

[118] C. Amiot, A. Aalto, P. Ryczkowski, J. Toivonen and G. Genty. "Cavity enhanced absorption spectroscopy in the mid-infrared using a supercontinuum source". *Applied Physics Letters* 111.6 (2017), p. 061103.

[119] Z. Eslami, P. Ryczkowski, C. Amiot, L. Salmela and G. Genty. "High-power short-wavelength infrared supercontinuum generation in multimode fluoride fiber". *JOSA B* 36.2 (2019), A72–A78.

[120] H. Tu and S. A. Boppart. "Coherent fiber supercontinuum for biophotonics". *Laser & photonics reviews* 7.5 (2013), pp. 628–645.

[121] Z. Eslami, L. Salmela, A. Filipkowski, D. Pysz, M. Klimczak, R. Buczynski, J. M. Dudley and G. Genty. "Two octave supercontinuum generation in a non-silica graded-index multimode fiber". *Nature Communications* 13.1 (2022), p. 2126.

[122] Z. Liu, L. G. Wright, D. N. Christodoulides and F. W. Wise. "Kerr self-cleaning of femtosecond-pulsed beams in graded-index multimode fiber". *Optics letters* 41.16 (2016), pp. 3675–3678.

[123] K. Krupa, A. Tonello, B. M. Shalaby, M. Fabert, A. Barthélémy, G. Millot, S. Wabnitz and V. Couderc. "Spatial beam self-cleaning in multimode fibres". *Nature Photonics* 11.4 (2017), pp. 237–241.

[124] J. Lægsgaard. "Spatial beam cleanup by pure Kerr processes in multimode fibers". *Optics letters* 43.11 (2018), pp. 2700–2703.

[125] T. Hansson, A. Tonello, T. Mansuryan, F. Mangini, M. Zitelli, M. Ferraro, A. Niang, R. Crescenzi, S. Wabnitz and V. Couderc. “Nonlinear beam self-imaging and self-focusing dynamics in a GRIN multimode optical fiber: theory and experiments”. *Optics Express* 28.16 (2020), pp. 24005–24021.

PUBLICATIONS

PUBLICATION
I

Short-range supercontinuum-based lidar for temperature profiling

A. Saleh, A. Aalto, P. Ryczkowski, G. Genty and J. Toivonen

Optics letters 44.17 (2019), pp. 4223–4226

DOI: 10.1364/OL.44.004223

Publication is licensed under a Creative Commons Attribution 4.0 International License CC-BY-NC-ND

Optics Letters

Short-range supercontinuum-based lidar for temperature profiling

ABBA SALEH,[1,2,*] **ANTTI AALTO,**[1] **PIOTR RYCZKOWSKI,**[1] **GOERY GENTY,**[1] **AND JUHA TOIVONEN**[1]

[1]*Photonics Laboratory, Physics Unit, Tampere University, P.O. Box 692, FI-33101 Tampere, Finland*
[2]*Valmet Technologies Oy, Energy Services, Lentokentankatu 11, P.O. Box 109, FI-33101 Tampere, Finland*
**Corresponding author: abba.saleh@tuni.fi*

Received 24 June 2019; revised 20 July 2019; accepted 1 August 2019; posted 1 August 2019 (Doc. ID 370849); published 22 August 2019

We developed a short-range light detection and ranging system using a supercontinuum (SC) source spectrally tailored to cover the ro-vibrational transition energies of desired components of a flue gas. The system enables remote measurements of the gas parameters, including temperature and concentration which play a key role in the performance of combustion power plants. The technique requires only one inspection window and, thus, can be used in combustion units with limited access. It exploits differential absorption between specific wavelength bands of the gas absorption spectrum. The transmittance of an individual wavelength band is derived from the detected backscattered temporal intensity of the SC pulses. We demonstrate water vapor temperature measurement in the range of 400°C–900°C in a laboratory furnace with the use of only two wavelength bands. Using more than two wavelength bands, the technique can be further extended to simultaneously measure temperature and concentration. By varying the direction of the incident beam in a non-parallel plane, a full 3D profile is also obtainable. © 2019 Optical Society of America

https://doi.org/10.1364/OL.44.004223

Provided under the terms of the OSA Open Access Publishing Agreement

Light detection and ranging (lidar) is a remote sensing technique [1] commonly used for the measurement of various atmospheric variables, including temperature, pressure, humidity, and trace gases concentration [1–6]. Lidar techniques have also been demonstrated for combustion diagnostics [7–10]. Typically, most of these methods are limited to the measurement of one species at a time as the laser wavelength is tuned to the absorption line of the investigated species. Recent advances in nonlinear fiber optics have led to the realization of spatially coherent and broadband light sources known as supercontinuum (SC) lasers. Under specific pumping conditions, the SC generation process exploits cascaded nonlinear dynamics resulting in highly directional broadband light [11]. This opens the door for simultaneous detection of multiple observables. Thus, supercontinuum light detection and ranging (SC-lidar) [12,13] and SC-based hyperspectral lidar [14,15] have shown great potential for simultaneous detection of multiple variables. To the best of our knowledge, an approach based on short-range (~1 – 10 m) SC-lidar for temperature measurement in combustion power plants is yet to be reported in the literature.

Temperature distribution inside a furnace is one of the main factors affecting the performance of combustion units (CUs). The ability to accurately measure the temperature inside a CU would pave the way for precise control and management of the combustion processes. Conventionally, thermocouples are used for temperature measurement in CUs [16]; however, this approach is inefficient because of its point-wise nature and ineffective for dynamic temperature monitoring due to the poor response of the thermocouple to fluctuating temperatures [17]. Other prior art solutions besides the lidar approach in Refs. [7–10] include spectroscopic methods such as thermometry based on thermographic phosphors [18], two-line thermometry employing wavelength modulation spectroscopy [19–21] and atomic fluorescence [22]. Another important technique is collinear photo fragmentation and atomic absorption spectroscopy, which utilizes chemical reaction kinetics to measure temperature [23]. The aforementioned promising optical spectroscopic methods detect signal transmitted through the examined space, thus requiring at least two openings in the furnace walls, which limits their detection area to the line between those openings.

Herein, we present a new method for non-intrusive combustion diagnostics based on an SC-lidar using just one opening. The approach is robust as the stringent requirement of a narrowband laser linewidth being precisely in tune with the absorption line of the probe gas, particularly in the aforementioned techniques, is mitigated by the broadband SC laser. The technique exploits the gas absorption cross-sectional dependence on temperature between wavelength bands. Consequently, the absorption strength of water vapor (H_2O) varies as a function of temperature, as shown in Fig. 1. We studied the temporal dynamics of H_2O temperatures in a laboratory furnace using just two wavelength bands. By measuring the temporal intensities of the backscattered SC light, the corresponding transmittance of individual wavelength band can be deduced, hence providing information indicative of differential absorption between the two wavelength bands. H_2O temperatures in the range of 400°C–900°C were inferred by comparing the transmittance ratio between these two wavelength bands.

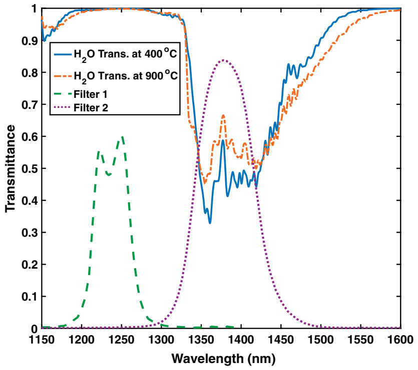

Fig. 1. Modeled H_2O transmittance spectra for two temperatures and an overlay of filter transmissions. Blue (—) and orange (- - -) are the H_2O transmittance spectra at 400°C and 900°C, respectively. Green (– –) and purple (.) are the corresponding filter transmissions for Ch1 and Ch2, respectively.

The SC-lidar signal (i.e., the detected back scattered signal) can be expressed as

$$S(t) = \frac{C_{\text{eff}}}{d_t^2}\int P_0(\lambda)\beta(\lambda)e^{\left(-\sigma(\lambda)\frac{N}{V}2l\right)}\mathrm{d}\lambda, \tag{1}$$

where $P_0(\lambda)$ is the initial spectrum of the SC laser; $\beta(\lambda)$ is the backscattering coefficient; C_{eff} is the collection efficiency; d_t is the distance travelled by the scattered light pulse at a given time t and can be obtained from the time of flight of the light pulse; l is the length of the absorbing medium, and the factor of two is attributed to the round trip by an SC light pulse; $\frac{N}{V}$ is the molecular number density and $\sigma(\lambda)$ is the wavelength-dependent absorption cross section (attenuation is considered to be only due to absorption). σ further depends on temperature via the line intensity in the spectrum and depends both on temperature and pressure via the line profile.

When two wavelength bands are used to probe flue gas parameters (as in Fig. 2), the corresponding signals detected at an individual wavelength band at a given time can be written as

$$S_1(t_1) = C_{\text{eff}1}\frac{\beta}{d_1^2}\int P_{01}(\lambda)\mathrm{d}\lambda, \tag{2}$$

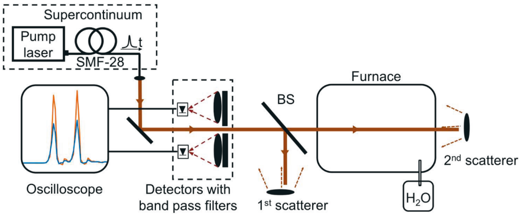

Fig. 2. Schematic diagram of the experimental setup. BS: beam splitter.

$$S_1(t_2) = C_{\text{eff}1}\frac{\beta}{d_2^2}\int P_{01}(\lambda)e^{\left(-\sigma_1(\lambda)\frac{N}{V}2l\right)}\mathrm{d}\lambda, \tag{3}$$

$$T_1 = \frac{S_1(t_2)}{S_1(t_1)} = \left(\frac{d_1}{d_2}\right)^2\frac{\int P_{01}(\lambda)e^{\left(-\sigma_1(\lambda)\frac{N}{V}2l\right)}\mathrm{d}\lambda}{\int P_{01}(\lambda)\mathrm{d}\lambda}, \tag{4}$$

where S_1 is the signal detected at the first wavelength band (Ch1); t_1 and t_2 are the times of flight of the light pulse in relation to the first and second scatterers, respectively; d_1 and d_2 are the corresponding distances travelled by the light pulse at the time t_1 and t_2; β is the backscattering coefficient, which is considered to be constant because the scatterers are large compared to the wavelength of the light; $C_{\text{eff}1}$, $P_{01}(\lambda)$, $\sigma_1(\lambda)$, and T_1 are the collection efficiency, initial spectrum of the SC, absorption cross section, and transmittance at Ch1, respectively. Similarly, the transmittance at the second wavelength band (Ch2) can be given as

$$T_2 = \left(\frac{d_1}{d_2}\right)^2\frac{\int P_{02}(\lambda)e^{\left(-\sigma_2(\lambda)\frac{N}{V}2l\right)}\mathrm{d}\lambda}{\int P_{02}(\lambda)\mathrm{d}\lambda}. \tag{5}$$

The transmittance ratio R of Ch2 to Ch1 is obtained by dividing Eq. (5) by (4):

$$R = \frac{\int P_{02}(\lambda)e^{\left(-\sigma_2(\lambda)\frac{N}{V}2l\right)}\mathrm{d}\lambda}{\int P_{02}(\lambda)\mathrm{d}\lambda}\,\frac{\int P_{01}(\lambda)\mathrm{d}\lambda}{\int P_{01}(\lambda)e^{\left(-\sigma_1(\lambda)\frac{N}{V}2l\right)}\mathrm{d}\lambda}. \tag{6}$$

Note that the process is self-calibrating, as the backscattering coefficients, as well as the collection efficiency of both Ch1 and Ch2 cancels out.

The transmission spectrum of H_2O, one of the main combustion products with a relatively high concentration and a rich absorption spectrum in the entire infrared, was thoroughly investigated. Specifically, the transmission spectrum of H_2O corresponding to a 100% concentration, a pressure of 1 atm, and an interaction length of about 1 m was modeled using the HITRAN 2012 database [24], as shown in Fig. 1. Note that the aforementioned H_2O parameters correspond to an equivalent optical thickness of the ideal power plant conditions. Typically 10% H_2O concentration, 10 m interaction length and a pressure of 1 atm. Based on the data presented in Fig. 1, two wavelength bands, namely, channel one (Ch1) and two (Ch2), were carefully selected. They are characterized by different responses of absorption to the temperature variation which allows for differential absorption measurement.

Figure 2 depicts the schematic of the experimental setup. The SC is generated by a cascaded Raman process in a 500 m long SMF-28 fiber (Thorlabs), pumped by KEOPSYS PYFL-KULT laser operating at 1064 nm and generating 2 ns long, 1 kW peak power pulses with a repetition rate of 280 kHz. The output spectrum of the source is presented in Fig. 3. SC light is collimated with a reflective collimator and guided towards ~1 m long quartz tube furnace containing 100% H_2O concentration at atmospheric pressure. Using a 50:50 beam splitter (BPD508-G, Thorlabs), part of the incident light is directed towards the 1st scatterer/diffuser (DG10-1500-P01, Thorlabs), placed just before the furnace. The rest of the beam traverses through the furnace undergoing absorption and, subsequently, scattered by the 2nd scatterer behind the furnace. In an ideal combustion environment, the role

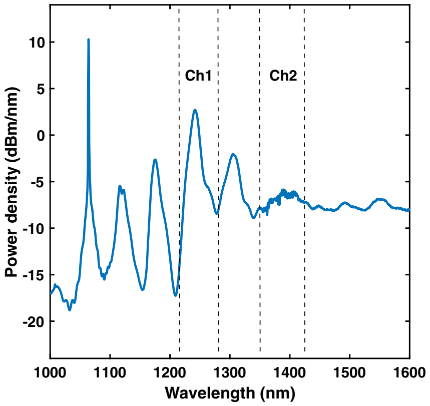

Fig. 3. SC spectrum and the corresponding FWHM position of the filters (Ch1 and Ch2) in the spectrum.

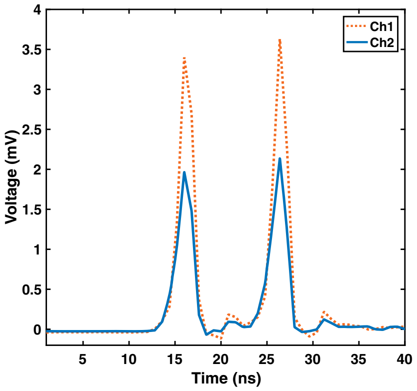

Fig. 4. Measured backscattered signals with no H_2O present in the furnace. The first and second peaks are the signals from the 1st and 2nd scatterers, respectively. The dotted line represents the Ch1 signal, while the solid line represents Ch2 signal.

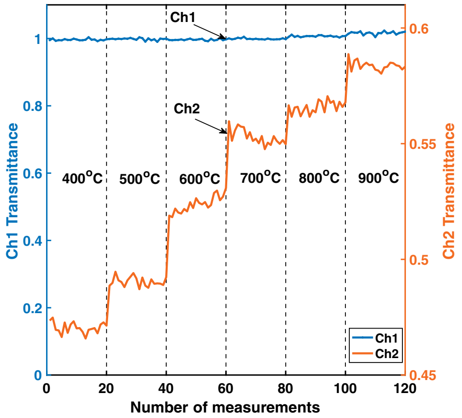

Fig. 5. Measured Ch1 (blue line) and Ch2 (orange line) transmittance with respect to furnace temperature. The measurement was carried out for a temperature range of 400°C–900°C, with 20 sets of measurement per temperature and each single measurement composing of 10,000 pulses.

of the scatterers is played by the naturally present aerosol particles which also provides sufficient scattering that enables signal detection over relatively long distances within the CU. Note that aerosol scattering is weak compared to that of the scatterers used in this experiment; hence, additional electronic pre-amplification of the signal will be required. The signal from the 2nd scatterer passes through the furnace again on the way back. The backscattered light from both scatterers is collected by two lens sets (AC254-030-C & AC254-075-C, Thorlabs) placed adjacent to each other, filtered by Ch1 and Ch2 filters (BP-1375-085 & BP-1240-050, Spectrogon) and focused on to the active area of two biased photodetectors (DET08C, Thorlabs). The temporarily resolved signal is recorded by a 12-bit oscilloscope (HDO6054, Lecroy). An example recorded signal is shown in Fig. 4.

The two distinct peaks separated in time represent the signals from the 1st and 2nd scatterers, respectively. The signal plotted in the figure is an average of 10,000 backscattered pulses, and the corresponding measurement time is about 40 ms. Furthermore, the measured temporal intensities of both channels are converted into individual channel transmittance using Eqs. (4) and (5). Figure 5 shows the measured transmittance of Ch1 and Ch2 at varying furnace temperatures of 400°C–900°C. The measurement at a given temperature composes 20 sets of measurement, with each measurement further composed of 10,000. Ch1 shows no change in transmittance with furnace temperature, while Ch2 shows an increase in transmittance with increasing furnace temperature, which is in good agreement with the modeled H_2O transmittance in Fig. 1. The standard deviation of the transmittance measurement, calculated based on 20 measurement repetitions of 10,0000 pulses, presented in Fig. 5 is 0.0024, with the mean value of transmittance ranging from 0.4704 to 0.5837, depending on the channel and temperature.

In order to infer the temperature of H_2O, the transmittance ratio R was calculated using Eq. (6). The mean value of all 20 measurements, which composes 200,000 pulses at a given temperature, was used in the calculation. The simulated and experimentally measured R as a function of the furnace temperature are compared in Fig. 6. We can see very good agreement between the simulated and experimentally measured ratios with a 50°C accuracy in the range 600°C–900°C. However, at lower furnace temperatures (400°C–500°C), the discrepancy between the simulated and measured ratios is more pronounced. This is because the quartz tube (i.e., the gas cell) extends a few centimeters outside the furnace heating zone on either sides of the furnace, thus creating a colder interface (i.e., temperature gradient) with respect to the internal part of the furnace (i.e., the heating zone). The colder region was measured to be less than 100°C. As a result, H_2O in these regions begins to condensate which yields additional loses on the beam

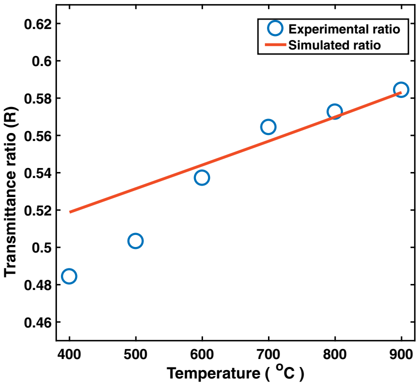

Fig. 6. Experimentally measured (circles) and simulated (solid line) transmittance ratios as a function of temperature.

path that are not accounted for in our model. Moreover, the temperature difference between the colder region and the heating zone was persistent, even at elevated furnace temperatures. Hence, the assumption of uniform H_2O temperature and concentration inside the furnace is partially violated by the presence of the colder regions in the test tube outside the furnace heating zone. Therefore, condensations of H_2O at lower furnace temperatures (400°C–500°C) coupled with the alteration of H_2O concentration due to interference from the colder regions at all furnace temperatures, have led to the observed discrepancies between the simulated and experimentally measured transmittance ratios in Fig. 6.

In summary, we have reported a novel technique based on a short-range SC-lidar for temperature measurement in CUs via a single opening. Water vapor with optical thickness equivalent to combustion power plant conditions was mimicked in a laboratory quartz tube furnace. H_2O temperatures were inferred from the transmittance ratio between two distinct wavelength bands. The measured and simulated H_2O temperatures were observed to be in a good agreement. The 2 ns duration of the spectrally filtered SC pulses should allow for a spatial resolution of about 30 cm with this technique in a case where scatterers are present all along the measurement path, as is the case in a combustion furnace. In addition, the SC pulses have significantly high peak power with a duty cycle of 0.0005, thus preventing any potential interference by thermal emissions such as black body radiations and chemiluminescence, from the furnace environment. Moreover, the same technique can be employed for simultaneous detection of temperature and concentration if multiple (i.e., more than two) wavelength bands of the SC spectrum are utilized in the combustion diagnosis, e.g., by adding an additional bandpass filter in the 1450–1550 nm spectral region. Finally, we emphasize that the technique possesses a great potential for simultaneous 3D mapping of both temperature and concentration, which can be achieved by varying the direction of the probe beam in a non-parallel plane.

Funding. Horizon 2020 Framework Programme (722380); Academy of Finland (320165).

REFERENCES

1. C. Weitkamp, *Lidar: Range-Resolved Optical Remote Sensing of the Atmosphere* (Springer, 2006), Vol. **102**.
2. S. H. Melfi, K. D. Evans, J. Li, D. Whiteman, R. Ferrare, and G. Schwemmer, Appl. Opt. **36**, 3551 (1997).
3. J. W. Hair, L. M. Caldwell, D. A. Krueger, and C.-Y. She, Appl. Opt. **40**, 5280 (2001).
4. G. Megie and R. T. Menzies, Appl. Opt. **19**, 1173 (1980).
5. Y. Zhao, Appl. Opt. **39**, 997 (2000).
6. J. L. Machol, T. Ayers, K. T. Schwenz, K. W. Koenig, R. M. Hardesty, C. J. Senff, M. A. Krainak, J. B. Abshire, H. E. Bravo, and S. P. Sandberg, Appl. Opt. **43**, 3110 (2004).
7. T. Leffler, C. Brackmann, A. Ehn, B. Kaldvee, M. Aldén, M. Berg, and J. Bood, Appl. Opt. **54**, 1058 (2015).
8. B. Kaldvee, A. Ehn, J. Bood, and M. Aldén, Appl. Opt. **48**, B65 (2009).
9. B. Kaldvee, J. Bood, and M. Aldén, Meas. Sci. Technol. **22**, 125302 (2011).
10. E. Malmqvist, M. Brydegaard, M. Aldén, and J. Bood, Opt. Express **26**, 14842 (2018).
11. J. M. Dudley, G. Genty, and S. Coen, Rev. Mod. Phys. **78**, 1135 (2006).
12. S. Kaasalainen, T. Lindroos, and J. Hyyppa, IEEE Geosci. Remote. Sens. Lett. **4**, 211 (2007).
13. G. Méjean, J. Kasparian, E. Salmon, J. Yu, J.-P. Wolf, R. Bourayou, R. Sauerbrey, M. Rodriguez, L. Wöste, H. Lehmann, B. Stecklum, U. Laux, J. Eislöffel, A. Scholz, and A. P. Hatzes, Appl. Phys. B **77**, 357 (2003).
14. Y. Chen, E. Räikkönen, S. Kaasalainen, J. Suomalainen, T. Hakala, J. Hyyppä, and R. Chen, Sensors **10**, 7057 (2010).
15. A. Manninen, T. Kääriäinen, T. Parviainen, S. Buchter, M. Heiliö, and T. Laurila, Opt. Express **22**, 7172 (2014).
16. D. Bradley and K. Matthews, J. Mech. Eng. Sci. **10**, 299 (1968).
17. M. Tagawa and Y. Ohta, Combust. Flame **109**, 549 (1997).
18. M. Aldén, A. Omrane, M. Richter, and G. Särner, Prog. Energy Combust. Sci. **37**, 422 (2011).
19. J. Liu, J. Jeffries, and R. Hanson, Appl. Phys. B **78**, 503 (2004).
20. X. Zhou, J. Jeffries, and R. Hanson, Appl. Phys. B **81**, 711 (2005).
21. G. B. Rieker, J. B. Jeffries, and R. K. Hanson, Appl. Opt. **48**, 5546 (2009).
22. J. Borggren, W. Weng, A. Hosseinnia, P.-E. Bengtsson, M. Aldén, and Z. Li, Appl. Phys. B **123**, 278 (2017).
23. J. Viljanen, T. Sorvajärvi, and J. Toivonen, Opt. Lett. **42**, 4925 (2017).
24. L. Rothman, I. Gordon, Y. Babikov, A. Barbe, D. C. Benner, P. Bernath, M. Birk, L. Bizzocchi, V. Boudon, L. Brown, A. Campargue, K. Chance, E. Cohen, L. Coudert, V. Devi, B. Drouin, A. Fayt, J.-M. Flaud, R. Gamache, J. Harrison, J.-M. Hartmann, C. Hill, J. Hodges, D. Jacquemart, A. Jolly, J. Lamouroux, R. L. Roy, G. Li, D. Long, O. Lyulin, C. Mackie, S. Massie, S. Mikhailenko, H. Müller, O. Naumenko, A. Nikitin, J. Orphal, V. Perevalov, A. Perrin, E. Polovtseva, C. Richard, M. Smith, E. Starikova, K. Sung, S. Tashkun, J. Tennyson, G. Toon, V. Tyuterev, and G. Wagner, J. Quant. Spectrosc. Radiat. Transf. **130**, 4 (2013).. HITRAN2012 special issue.

130.230.127.154 {ts '2023-01-11 03:56:27'}

PUBLICATION
II

Supercontinuum lidar for industrial process analysis

A. Saleh, P. Ryczkowski, G. Genty and J. Toivonen

Optics Express 29.25 (2021), pp. 42082–42089

DOI: 10.1364/OE.443244

Publication is licensed under a Creative Commons Attribution 4.0 International License CC-BY-NC-ND

Research Article Vol. 29, No. 25 / 6 Dec 2021 / Optics Express 42082

Optics EXPRESS

Supercontinuum lidar for industrial process analysis

ABBA SALEH,[1,2,*] PIOTR RYCZKOWSKI,[1] GOERY GENTY,[1] AND JUHA TOIVONEN[1]

[1] *Photonics Laboratory, Physics Unit, Tampere University, P.O. Box 692, FI- 33101 Tampere, Finland*
[2] *Valmet Technologies Oy, Energy Services, Lentokentankatu 11, P.O. Box 109, FI- 33101 Tampere, Finland*
[*] *abba.saleh@tuni.fi*

Abstract: Real-time monitoring of flue gas parameters in combustion processes is central to the optimization of the process efficiency and reduction of pollutants emission. We report simultaneous measurement of the average water vapor temperature and concentration over a 9 m distance in a full-scale industrial boiler by broadband lidar employing a custom supercontinuum source covering the wavelengths of ro-vibrational absorption of water molecules at 1.2 – 1.55 µm. The measured average temperature and concentration are in excellent agreement with reference measurements. We also take advantage of the backscattering from the aerosol particles present in the boiler to map the water vapor concentration profile in the boiler up to a distance of 2.7 m with a spatial resolution of 30 cm. Our results open novel perspectives for 3D profiling of temperature and gas concentration in industrial environments.

© 2021 Optical Society of America under the terms of the OSA Open Access Publishing Agreement

1. Introduction

Global energy demand has tremendously increased over the years, raising environmental concerns. This has led to new energy policies aiming towards renewable energy alternatives and zero net CO_2 fuels such as biomass. The performance of a combustion power plant relies on the internal distribution of its flue gas parameters, such as the temperature and molecular concentrations, and accurate profiling of these parameters would pave the way for optimized combustion process control, increased energy production efficiency and lower emissions.

Conventional approaches for the measurement of flue gas temperature and concentration rely on thermocouple [1] or Fourier transform infrared (FTIR) spectroscopy [2,3]. However, both techniques are inefficient in terms of pointwise measurements. Moreover, the FTIR approach is extractive in nature, yielding significant challenges (latency, moisture content in the gas and ash in the furnace) which makes real-time monitoring of the combustion processes particularly difficult. Flue gas temperature monitoring with a thermocouple is inapplicable to in-situ temperature probing due to the long time constant of the thermocouple response [4] relative to the dynamic temperature distribution of the flue gas. Other optical spectroscopic techniques have been proposed for combustion diagnostics [5–8], however, these typically measure the transmitted signal across a given path between two openings in the furnace walls limiting the measurement area and making them not well-suited to combustion units with limited optical access such as boilers.

Lidar technologies offer novel perspectives for industrial process control and combustion diagnostics. Lidar operation principle is based on time of flight measurement of backscattered electromagnetic radiation [9], enabling remote characterization of flue gas parameters with high spatial resolution [10–12]. Lidar techniques typically use a narrowband laser tuned to the absorption line of the gas of interest, which restricts measurements to a single gas specie. In this context, the development of spatially coherent broadband supercontinuum (SC) light source [13] has opened up new possibilities for simultaneous detection of multiple parameters of flue gas components as shown in a recent demonstration of a laboratory-scale combustion study [14].

#443244 https://doi.org/10.1364/OE.443244
Journal © 2021 Received 13 Sep 2021; revised 16 Nov 2021; accepted 22 Nov 2021; published 2 Dec 2021

Here, we report real-time combustion diagnostics in a full-scale 9-m-wide industrial boiler via single optical access using a SC-lidar system. Exploiting differential absorption SC spectrum, we demonstrate simultaneous measurement of water vapor temperature and concentration. The average water vapor concentration and temperature are determined using the strong backscattering from the back wall of the boiler. Taking advantage of the backscattering from the aerosol particles naturally present in the boiler, we further map the water vapor concentration along the beam path up to 2.7 m with a resolution of 30 cm limited by the signal-to-noise ratio and SC pulse duration, respectively. Our results demonstrates the unique capability of SC-lidar for diagnosis in combustion units and other industrial environments and open up novel perspective for 3D profiling of temperature and gas concentration in industrial environments.

2. Methodology

We begin by illustrating the temperature and concentration measurement principle of water vapor (H_2O) which is one of the primary flue gas component in a biomass combustion boiler. The transmission spectrum of H_2O in the near-infrared with a typical 20 % concentration, pressure of 1 atm and for an interaction length of 9 m was modeled with high spectral resolution using the HITEMP database [15]. Figure 1 shows the transmission spectrum for two different temperature (400 °C and 900 °C) convoluted to a low spectral resolution for better visualization. One can see how the transmittance depends on the temperature, and this can be advantageously used to determine the gas temperature using three spectral regions as highlighted in the figure: Channel 1 (Ch1), Channel 2 (Ch2), and Channel 3 (Ch3) have corresponding central wavelengths of 1240 nm, 1375 nm and 1500 nm, and full width half maximum (FWHM) of 50 nm, 85 nm and 90 nm respectively. Ch1 is used as a reference channel with negligible water vapor absorption, Ch2 and Ch3 wherein light experiences significant water vapor absorption and which can be used to determine the temperature as described below.

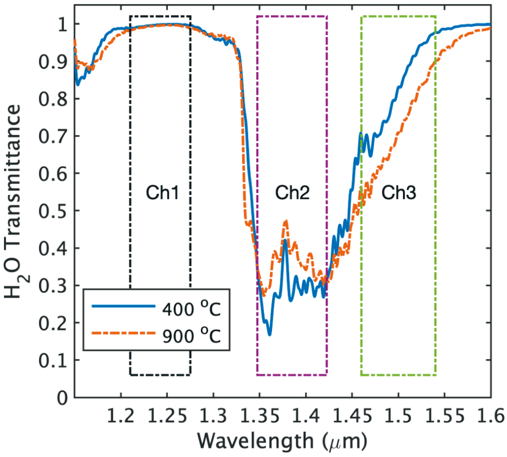

Fig. 1. Modeled H_2O transmittance spectra at two extreme temperatures observed inside a boiler furnace and an overlay of the corresponding wavelength ranges of three specific bandpass filters Ch1, Ch2 and Ch3. Blue (—) and orange (- -) lines are the H_2O transmittance spectra at 400 °C and 900 °C, respectively.

The backscattered signal $S_n(t_m)$ from Channel $n = 1, 2, 3$ detected after a time of flight t_m can be expressed as [9]

$$S_n(t_m) = \frac{C_{\text{eff}}\beta_m}{{d_m}^2} \int_{\Delta\lambda_n} P_0(\lambda)\Gamma_n(\lambda) \exp\left[-2\sum_{k=1}^{m} \frac{N_k}{V_k}\sigma_k(\lambda, T)\Delta l_k\right] d\lambda, \tag{1}$$

where $\Delta\lambda_n$ is the spectral interval of Channel $n = 1, 2, 3$, d_m is the distance travelled by the backscattered light during time t_m, C_{eff} is the collection efficiency, and β_m is the backscattering coefficient (considered to be wavelength independent as the technique utilizes a relatively small wavelength range of 1.2 – 1.55 µm). The main scattering source is the combustion related fly ash aerosol particles with dimension much larger than the wavelength. $P_0(\lambda)$ is the initial spectrum of the SC source, $\Gamma_n(\lambda)$ is the filter transmission for channel n, and $\sigma(\lambda, T)$ is the absorption cross section dependent on wavelength and gas temperature. $\frac{N_k}{V_k}$ is the molecular number density of the probed gas. The travelled path d_m is divided into elementary segments wherein the temperature and concentration is assumed to be constant. The minimum length of each segment $\Delta l_k = c\tau/2$ is determined by the SC pulse duration τ (c is the speed of light). The first segment parameters are calculated using the initial spectrum of the light source $P_0(\lambda)$. The second segment transmission calculation requires the initial spectrum to be modified by the absorption it experienced in the first segment and the process is then iteratively repeated as the absorption of all preceding segments is known. The total transmittance of individual channels within a given segment can be calculated from

$$T_{n,m} = \frac{S_n(t_{m+1})}{S_n(t_m)}, \tag{2}$$

where $S_n(t_{m+1})$ and $S_n(t_m)$ are the measured backscattered signal at time t_{m+1} and time t_m, respectively. Taking the ratio of transmittance between two different channels does cancel out the effect of d_m^2, C_{eff}, and β_m from the SC-lidar equation assuming that their wavelength dependence is negligible at our operation wavelengths. Knowing the absorption cross section, the light source spctrum as well as the filter transmission spectrum is sufficient to simulate the measured transmittance ratios. The simulated transmittance ratios are formulated to comprise an array of values, calculated using the HITEMP database, and varying temperature and concentration of the gas. The probed gas temperature and concentration are then deduced by fitting the simulated transmittance ratios to the measured ratios using

$$\Delta_{21,m} = \left|\frac{T_{2,m}}{T_{1,m}} - \frac{T_{2,Sim}}{T_{1,Sim}}\right| \tag{3}$$

$$\Delta_{31,m} = \left|\frac{T_{3,m}}{T_{1,m}} - \frac{T_{3,Sim}}{T_{1,Sim}}\right|, \tag{4}$$

where Δ_{21} and Δ_{31} are the resulting difference between the measured and simulated transmittance ratios of Ch2 to Ch1 and Ch3 to Ch1, respectively. Δ_{21} and Δ_{31} are numerically computed based on the simulations and the measured data, and the minimum error point corresponds to the resulted temperature and concentration of the probed gas.

3. Experiment

Measurements were performed at a 9-m-wide fluidized bed biomass boiler with 190 MW thermal power. A schematic illustration of the experiments is shown in Fig. 2. The light source is a SC generating 2-ns-long pulses with 1 kW peak power and repetition rate of 280 kHz (more detailed can be found in Ref. 13). The SC light is collimated with a reflective collimator and directed to the sidewall of the boiler comprising an opening (hatch). Multiple combustion gases including CO_x, NO_x, H_2O and CH_4 are present in the boiler as well as aerosol particles distributed throughout the entire volume. The SC light is scattered by the aerosol particles and partially absorbed by the H_2O molecules as it propagates through the boiler. The inside of the furnace walls is covered with soot which strongly scatters the rest of the beam upon incidence on the back end wall. The backscattered light is collected via a receiver telescope lenses (AC508-075-C & AC254-030-C, Thorlabs) and split using a 50:50 beam splitter (BPD254S-G, Thorlabs). Light transmitted by the beam splitter is spectrally filtered into Ch2 (BP-1375-085, Spectrogon) and focused onto a photodetector (ET-3070, EOT). The reflected light by the beam splitter is splitted using another identical beam splitter and spectrally separated into Ch1 and Ch3 with appropriate filters (BP-1240-050 & BP-1500-090, Spectrogon). The bandpass filters are

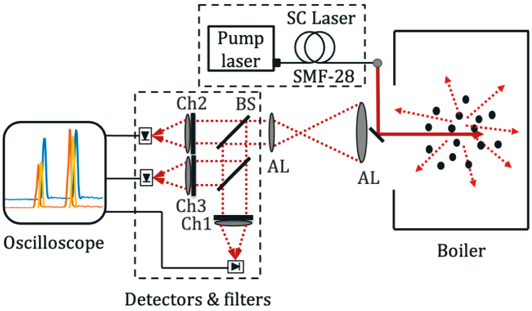

Fig. 2. Layout of experimental arrangement. Abbreviation AL stands for Achromatic Lens, SMF for Single Mode Fiber and BS for Beam Splitter. Ch1, Ch2 and Ch3 are the corresponding bandpass filters for channel 1, 2 and 3, respectively.

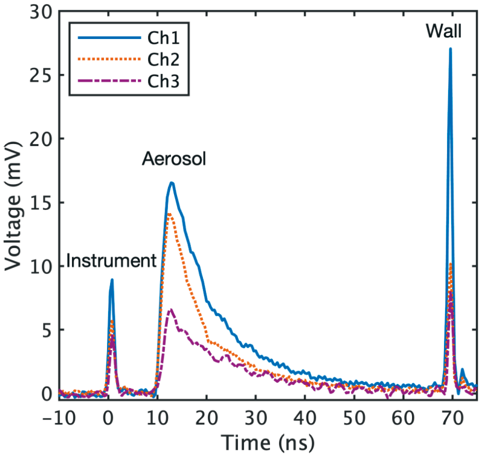

Fig. 3. Measured backscattered SC-lidar signal from a full-scale industrial boiler. The blue (—), orange (· · ·) and purple (- -) lines represent the signals for Ch1, Ch2 and Ch3 respectively. The first and last sharp peaks in the signal corresponds to scattering from the SC source input coupler and the boiler back wall respectively. The signal recorded between 10 ns and 60 ns originates from scattering by the aerosol particles.

having optical density of 3 at the blocking wavelengths. The corresponding signals are measured with identical photodetectors. The time window of signal collection is triggered by an optical pulse generated by the laser, eliminating the influence of the laser pulse emission time jitter. The signal from each photodetector is preamplified by an electronic amplifier (HSA-Y-1-60, FEMTO) and the temporarily resolved signal is recorded by a 12-bit oscilloscope (HDO6054, Lecroy). Note that SC pulse scattered from different positions inside the furnace arrives at the detector with different time delays, thus encoding spatial dimension onto the temporal signal. An example of recorded signal is shown in Fig. 3. The signal was averaged over sixty-five thousand backscattered pulses recorded over a total measurement time of about 230 ms. Identical measurement time and averaging was used in all our measurements. One can see that the detected signal exhibits three different peaks at different delay times. The first peak in the detected signal near zero-delay represents scattering from the coupling mirror placed in front of the boiler. The broad and slowly decaying peak near 10 ns represents the scattered signal from the aerosol particles. The third peak at around 70 ns delay originates from the boiler back wall reflection.

4. Results and discussion

The average temperature and H_2O concentration in the boiler can be determined from the first (coupling mirror) and last (boiler wall) backscattering peaks of the recorded signal in Fig. 3. The total transmittance across the boiler is derived for the three channels using Eq. (2). Corresponding gas temperature and concentration are then extracted from Eq. (3) and Eq. (4) with solutions for Channel 2 to 1 and 3 to 1 transmission ratios (with respect to simulation) shown in Fig. 4. The global solution is then found at the point of intersection between Δ_{21} and Δ_{31}, yielding 890°C and 20.3% for the average temperature and concentration of the water vapor, respectively. The standard deviation based on 20 consecutive measurement is 50 °C and 0.8 % for the temperature and concentration respectively.

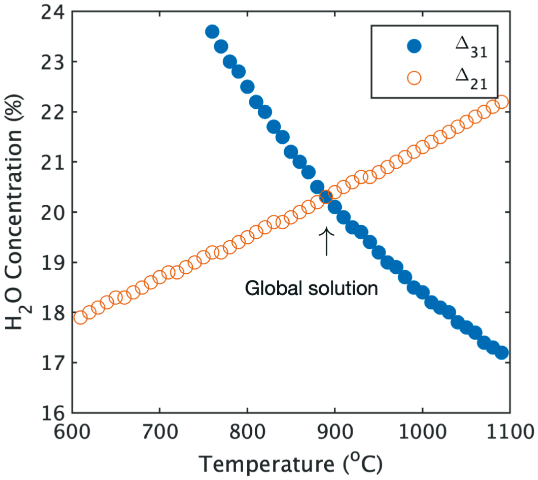

Fig. 4. Minimum error solutions for the difference between the measured (with SC-lidar) and simulated transmittance ratios Δ_{21} and Δ_{31}. Orange (circle) and blue (dot) represents Δ_{21} and Δ_{31} respectively. The global solution can be found at the point of intersection between Δ_{21} and Δ_{31}.

In order to evaluate the accuracy of our SC-lidar measurements, the results were compared with that of a reference measurement performed using a K-type thermocouple with a maximum penetration depth of about 1.5 m and a 1.045 radiative correction coefficient and the results are shown in Table 1. The estimated average boiler temperature from the thermocouple is 850 °C. The average water vapor concentration was estimated via heat and mass balance calculation [16] utilizing the biomass fuel moisture content measured from oven drying and based on the ISO 18134-3:2015 standard. The resulting average H_2O concentration in the furnace was in the range of 20 – 25 %. These reference measurements agrees very well with the SC-lidar results. It is also important to emphasize that the accuracy of the SC-lidar measurements is perfectly sufficient for industrial-scale process monitoring.

Table 1. Comparison between the reference and SC-lidar measured average temperature and H_2O concentration values in the boiler.

Measurement	Temperature (°C)	H_2O Concentration (%)
Reference	850	20 – 25
SC-lidar	890	20.3

One can take advantage of the backscattered signal from the aerosol particles to spatially resolve the variations in the water vapor temperature and concentration. For this purpose, the measured backscattering signal shown in Fig. 3 is split into discrete segment of 30 cm and the transmittance of each individual segment is derived using Eq. (2). Spatially resolving the gas temperature is infeasible with the current data due to poor signal-to-noise ratio. However, one can solve for the concentration values of the gas by assuming a known temperature, as the relative change in transmission due to temperature variation within a given segment is approximately equivalent to the noise amplitude of the measured signal. Using the reference temperature value of 850 °C across all segments, the H_2O concentration profile in the boiler can be spatially resolved using Eq. (3). The histogram in Fig. 5 shows the retrieved H_2O concentration profile as a function

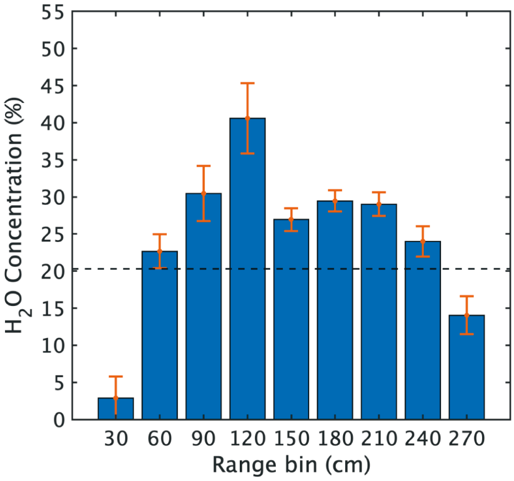

Fig. 5. Spatially resolved H_2O concentration profile and an overlay (– -) of the SC-lidar measured average H_2O concentration in the boiler.

of distance with the measured average H_2O concentration across the boiler marked as the dashed line. The error bar in the histogram was calculated from twenty consecutive measurements. The measured intensities had about 2 % variation between the measurements. The H_2O concentration values are resolved up to a distance 270 cm into the boiler. Spatially resolving the concentration values at longer distances is limited by the current signal-to-noise ratio of our detection. One can see from Fig. 5 that the H_2O concentration distribution is typically low towards the boiler wall. The hatch (inlet) was kept open during the measurement resulting in mixing with the surrounding air, which in turn alters the initial concentration as well as temperature of the gas at close proximity to the wall.

5. Conclusion and outlook

We have demonstrated robust real-time monitoring of combustion gases using a supercontinuum-lidar. The technique enables simultaneous remote measurement of the gas temperature and concentration via single optical access. Proof-of-concept measurements was demonstrated in a full-scale industrial boiler using three specific wavelength bands in the supercontinuum spectrum. Average temperature and concentration distribution of water vapor across the boiler could be measured with a statistical accuracy of 50 °C and 0.8 %, respectively, which is sufficient for industrial-scale process monitoring. The water vapor concentration profile was further spatially resolved with 30 cm resolution up to a 2.7 m distance inside the boiler, limited by the signal-to-noise ratio. The signal-to-noise ratio also did not allow to spatially resolve the gas temperature as the temperature induced change in transmittance within a given segment is of the same order of magnitude as the noise amplitude. The main origin of noise in this experiment is attributed to the SC source spectrum instabilities, and the readout noise associated with the detectors, amplifiers as well as the oscilloscope. Nevertheless, these challenges can be overcome by optimizing the data acquisition scheme to enhance the signal-to-noise ratio. Specifically, this can be achieved using a fast digitizer with real-time processing capability, enabling continuous averaging of the SC pulses at the repetition rate of the laser as well as by employing a SC source with higher spectral power density. Finally, we emphasize the unique potential of the technique for simultaneous 3D profiling of flue gas temperature and molecular concentrations, which can be realized by steering the incident probe beam using a single opening in a boiler or other similar industrial environment.

Funding. Academy of Finland (320165); Horizon 2020 Framework Programme (722380).

Acknowledgments. A.S acknowledges the support from Finnish Cultural Foundation. The authors would like to express their sincere gratitude to Jaani Silvennoinen and Jari Perälä for organizing the measurement campapaign, and Tampereen Sähkölaitos for making these experiments possible by granting us access to their power plant.

Disclosures. The authors declare no conflicts of interest.

Data availability. Data underlying the results presented in this paper are not publicly available at this time but may be obtained from the authors upon reasonable request.

References

1. D. Bradley and K. Matthews, "Measurement of high gas temperatures with fine wire thermocouples," J. Mech. Eng. Sci. **10**(4), 299–305 (1968).
2. E. Vainio, A. Brink, M. Hupa, H. Vesala, and T. Kajolinna, "Fate of fuel nitrogen in the furnace of an industrial bubbling fluidized bed boiler during combustion of biomass fuel mixtures," Energy & fuels **26**(1), 94–101 (2012).
3. E. Vainio, *Fate of fuel-bound nitrogen and sulfur in biomass-fired industrial boilers* (Åbo Akademi University, PhD thesis, 2014).
4. M. Tagawa and Y. Ohta, "Two-thermocouple probe for fluctuating temperature measurement in combustion–rational estimation of mean and fluctuating time constants," Combust. Flame **109**(4), 549–560 (1997).
5. X. Zhou, J. Jeffries, and R. Hanson, "Development of a fast temperature sensor for combustion gases using a single tunable diode laser," Appl. Phys. B **81**(5), 711–722 (2005).
6. M. Aldén, A. Omrane, M. Richter, and G. Särner, "Thermographic phosphors for thermometry: a survey of combustion applications," Prog. Energy Combust. Sci. **37**(4), 422–461 (2011).

7. J. Borggren, W. Weng, A. Hosseinnia, P.-E. Bengtsson, M. Aldén, and Z. Li, "Diode laser-based thermometry using two-line atomic fluorescence of indium and gallium," Appl. Phys. B **123**(12), 278 (2017).
8. J. Viljanen, T. Sorvajärvi, and J. Toivonen, "In situ laser measurement of oxygen concentration and flue gas temperature utilizing chemical reaction kinetics," Opt. Lett. **42**(23), 4925–4928 (2017).
9. C. Weitkamp, ed., *Lidar: Range-Resolved Optical Remote Sensing of the Atmosphere*, vol. 102 of *Springer Series in Optical Sciences* (Springer, 2005).
10. B. Kaldvee, J. Bood, and M. Aldén, "Picosecond-lidar thermometry in a measurement volume surrounded by highly scattering media," Meas. Sci. Technol. **22**(12), 125302 (2011).
11. E. Malmqvist, J. Borggren, M. Aldén, and J. Bood, "Lidar thermometry using two-line atomic fluorescence," Appl. Opt. **58**(4), 1128–1133 (2019).
12. E. Malmqvist, M. Brydegaard, M. Aldén, and J. Bood, "Scheimpflug lidar for combustion diagnostics," Opt. Express **26**(12), 14842–14858 (2018).
13. J. M. Dudley, G. Genty, and S. Coen, "Supercontinuum generation in photonic crystal fiber," Rev. Mod. Phys. **78**(4), 1135–1184 (2006).
14. A. Saleh, A. Aalto, P. Ryczkowski, G. Genty, and J. Toivonen, "Short-range supercontinuum-based lidar for temperature profiling," Opt. Lett. **44**(17), 4223–4226 (2019).
15. L. Rothman, I. Gordon, R. Barber, H. Dothe, R. Gamache, A. Goldman, V. Perevalov, S. Tashkun, and J. Tennyson, "Hitemp, the high-temperature molecular spectroscopic database," J. Quant. Spectrosc. Radiat. Transfer **111**(15), 2139–2150 (2010).
16. K. C. Weston, *Energy Conversion* (PSW Publishers, 1992), Chap. 3.

130.230.127.154 {ts '2023-01-11 03:58:48'}

PUBLICATION
III

Mid-infrared hyperspectral sensor based on MEMS Fabry-Pérot interferometer for stand-off sensing applications

A. Saleh, M. Mekhrengin, T. Dönsberg, T. Kääriäinen, G. Genoud and J. Toivonen

Scientific Reports 12.1 (2022), pp. 1–6

DOI: 10.1038/s41598-022-23758-w

Publication is licensed under a Creative Commons Attribution 4.0 International License CC-BY-NC-ND

www.nature.com/scientificreports

scientific reports

OPEN

Mid-infrared hyperspectral sensor based on MEMS Fabry-Pérot interferometer for stand-off sensing applications

Abba Saleh[1]✉, **Mikhail Mekhrengin**[2], **Timo Dönsberg**[2], **Teemu Kääriäinen**[2], **Guillaume Genoud**[2] & **Juha Toivonen**[1]

We report a novel hyperspectral sensor employing a Fabry-Pérot interferometer based on micro-electro-mechnical system and a custom mid-infrared supercontinuum laser. The Fabry-Pérot interferometer allows on-axis filtering, of spectral components of supercontinuum light backscattered from a target, with a spectral resolution of about 25 nm. We demonstrated hyperspectral identification of black polypropylene (PP) and polyethylene (PE500) using the 3–3.5 μm region of the supercontinuum spectrum and a corresponding measurement rate of 62.5 spectra / s. The resulted spectra show excellent agreement with the reference based on an FTIR spectrometer. Furthermore, we showed that the coloring of the plastics has no effect on their identification at this wavelength range.

A hyperspectral sensor measures transmitted or backscattered light from a target, probing multiple spectral components of the light to enable analysis of the target. Hyperspectral sensors have been widely used in various applications including agriculture[1], medicine[2] and mineral exploration[3]. Conventional hyperspectral sensors and cameras rely on passive target illumination, typically ambient lightening, which make them prone to misinterpretation due to any fluctuations in the illumination spectrum as it undermines the integrity of the signal. However, recent advances in nonlinear fiber optics have led to the development of spatially coherent yet broadband fiber lasers, termed supercontinuum (SC) lasers[4,5], enabling active target illumination for robust multi-spectral[6,7] as well as hyperspectral[8–10] sensing applications with very high signal-to-noise ratio.

Furthermore, significant progress in terms of the SC spectrum expanding into the mid-infrared (MIR), have been reported in the literature[11,12], with significantly high average output power[13], high repetition rate[14] and femtosecond pulse durations[15,16], opening the door for various applications in the MIR including spectroscopy[17], imaging[18] and optical coherence tomography (OCT)[19]. The MIR spectral region offers novel perspective for a more accurate analysis of a target as molecules demonstrate strong and characteristic absorption in this region, termed the molecular fingerprint, due to the strong fundamental vibrational transitions[20]. The aforementioned properties of MIR SC have opened up new possibilities for hyperspectral sensing applications in the MIR spectral region. However, a fast and robust filtering of various spectral components of the MIR SC spectrum is required to meet the demands of hyperspectral sensing applications. Some promising solutions based on a spectrometer comprising a miniaturized Fabry-Pérot interferometer have been proposed in the literature[8]. However, the integrated nature of the spectrometer limits the sensor design flexibility and photodetector choice as both the detector and the Fabry-Pérot interferometer are incorporated as a single unit. Thus, further study is required to fully realize the commercial potential of MIR hyperspectral sensors.

Herein, we present an active hyperspectral sensor (AHS) using a combination of a MEMS-based Fabry-Pérot interferometer (FPI) and a spectrally tailored SC light source covering up to 3.5 μm of the MIR spectral region. The voltage tunable FPI enables compact, cost effective and on axis non-dispersive filtering of spectral components of the SC light reflected from a target. The standalone nature of the FPI allows flexible instrument design as it can be placed at any desirable location on the instrument. We showed for the first time, to the best of our knowledge, the suitability of FPI for hyperspectral sensing of plastics. We demonstrated hyperspectral identification of black plastics as their detection is tedious in the near infrared (NIR) due to the carbon based additives which significantly absorb the NIR light. Black polyethylene (PE500) and polypropylene (PP) are specifically

[1]Photonics Laboratory, Tampere University, Tampere 33101, Finland. [2]VTT Technical Research Centre of Finland Ltd, Espoo 02150, Finland. ✉email: abba.saleh@tuni.fi

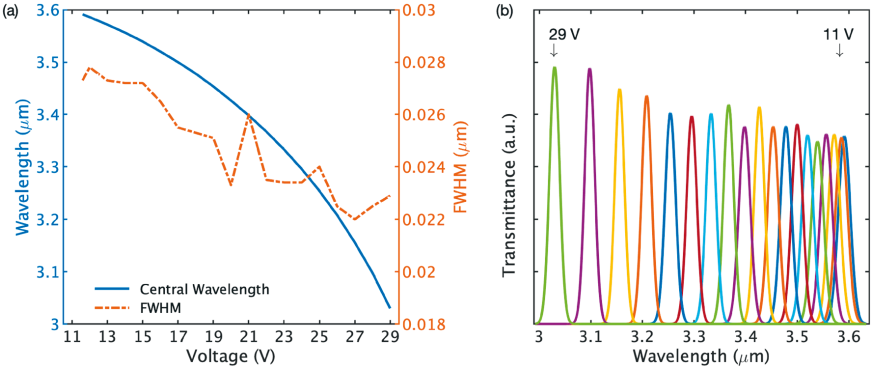

Figure 1. Tuning parameters of the Fabry-Pérot interferometer. (**a**) The blue line represents the corresponding central wavelength with respect to the tuning voltage, and the overlay red (dashed) line shows the full-width-half-maximum (FWHM). (**b**) Transmittance spectra of the Fabry-Pérot interferometer are shown as a function of the operating voltage in the range of 11–29 V with constant voltage increments indicated by different colors in the figure.

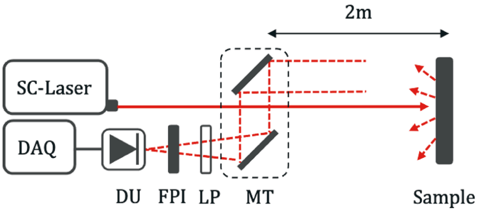

Figure 2. Experimental setup for stand-off hyperspectral reflectance measurement. Abbreviations: MT—mirror telescope, LP—longpass filter, DU—detection unit, FPI—Fabry-Pérot interferometer and DAQ—data acquisition.

chosen as sample materials as they are one of the most important black plastic waste especially among waste electrical and electronic equipment (WEEE)[21]. Additionally, they have very similar absorption features which makes them very difficult to distinguish. We successfully measured their reflectance spectra using the $3-3.5\ \mu m$ spectral band of the SC spectrum. The resulting spectra strongly correspond to their reference based on an FTIR spectrometer. The technique is further extended to detection of white plastics to validate its applicability to differently colored plastics. This emphasizes the great potential of the technique for plastic wastes sorting, in recycling processes, and other hyperspectral sensing applications.

Methods and results

Operational parameters of the Fabry-Pérot interferometer are shown in Fig. 1. The miniaturized MEMS-based tunable FPI filter is part of the MEMS-FPI solutions developed at VTT Technical Research Centre of Finland Ltd[22–25]. The FPI resonator comprises two highly reflective mirrors separated by an air gap. Constructively interfered light between the mirrors is transmitted, and the transmission band is defined by the air gap between the mirrors. The air gap is tuned by applying a voltage between the mirrors and, thus, the transmission band of the FPI can be tuned to the range of interest. Figure 1a presents the tuning parameters of the FPI. The operating voltage of the FPI is in the range of 0 – 29 V which corresponds to a wavelength tuning range of 3000 – 3600 nm. The full width half maximum (FWHM) of the transmission band remains in the range of 22 – 28 nm over the whole operating range of the FPI. An example transmittance spectra of the FPI at a constant voltage increment is shown in Fig. 1b.

The experimental arrangement is presented in Fig. 2. A custom SC light source[26] producing 10 kW peak power sub-nanosecond pulses at a repetition rate of 100 kHz (more detailed description of the supercontinuum light source can be found in Ref. 26) is directed towards a black plastic target having a thickness of 3–5 mm and located at a distance of 2 m. The SC light is partially absorbed upon incidence on the target while being scattered. The backscattered light is collected via a mirror telescope arrangement (MPD399V–M01 & PFE10–P01, Thorlabs) then filtered by a longpass filter (SLWP-2989-000453,NOC) to cut out wavelengths below 3000 nm.

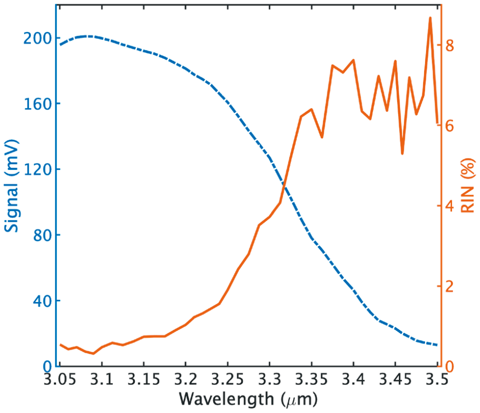

Figure 3. Measured backscattered SC spectrum (– -) from a diffuser and the corresponding relative intensity noise (—) based on ten consecutive measurements.

The FPI scans across 3050–3600 nm spectral range at a frequency of 62.5 Hz. The light transmitted through the FPI is focused onto a photodetector (PV-3TE-5, VIGO Systems). The measured signal is amplified with a custom bandpass-filtered amplifier having a voltage gain of 250 and passband of 3.5 kHz - 10 MHz. The measured sub-nanosecond SC pulses are temporarily stretched due to the 10 MHz cut-off frequency of the amplifiers. They are digitized using a 14-bit analog-to-digital converter (LTC2145-14, Analog Devices, Inc.) which is a part of a development board (STEMlab 125-14, Red Pitaya d.d.). The digitized signal is processed using a system on a chip (SoC) solution (Zynq 7010, Xilinx). The SoC contains field-programmable gate array (FPGA)-based programmable logic (Artix 7, Xilinx) and a processor (ARM Cortex-A9 MPCore, Arm Holdings). The FPGA part of SoC removes constant component of the signal and integrates all data samples related to one SC pulse into one value while the processor send the integrated data values to the PC via Ethernet. The FPI voltage modulation and SoC acquisition software are synchronized using the same external trigger as applied for the SC laser. Although the FPI scans continuously during the measurement, the measured spectra seem to show discrete values as transmitted signal is sampled by FPGA with 125 MHz-sampling rate, which allows to distinguish and integrate individual SC pulses. And they are then averaged over 100-µs-long periods of time, corresponding to independent spectral channels.

The reflectance spectrum of a sample can be derived using

$$R = \frac{I_S - N}{I_R - N}, \tag{1}$$

where I_S and I_R are the measured intensity spectrum of the sample and reference target respectively, and N is the background noise. As a reference target, we used a ground glass diffuser (DG10-120-M01, Thorlabs) having spectrally flat reflectance of 97.5 % over the probed wavelength range.

Figure 3 shows a measured backscattered SC spectrum from the diffuser and the corresponding relative intensity noise (RIN) based on 10 different measurements. The resulted spectral shape is mainly due to the spectrum of the SC light source, as the diffuser and detector responses are flat over the probed wavelength range. The RIN is calculated from 10 consecutive measurements, where a single measurement is an average of two-hundred spectra corresponding to a measurement time of 3.2 s and an average of a thousand pulses per spectral channel. The relative intensity variations between subsequent measurements can reach values as small as 1 % at the wavelength of 3 μm and increases to about 8 % at the wavelength of 3.5 μm. The dramatic variation in the 3.35–3.5 μm region, which coincides with the long wavelength edge of the SC spectrum, is attributed to the significant decrease in the power spectral density and large stochastic spectral power fluctuation of the SC source. These intensity fluctuations are typical characteristics at both the short and long wavelength edges of a supercontinuum spectrum[27].

A black polypropylene (PP) sample is investigated using the developed active hyperspectral sensor (AHS), and its corresponding reflectance is obtained using Eq. 1. The resulted spectrum is compared to a reference black PP reflectance spectrum measured with an FTIR spectrometer (FT-MIR Rocket, ARCoptix) having a spectral coverage of 2–6 μm and a resolution of 4 cm^{-1}. The comparison of the black PP reflectance spectra, measured with both the AHS and the FTIR spectrometer, is shown in Fig. 4a. The FTIR and AHS spectra demonstrate a very close agreement. The two reflectance peaks in the FTIR spectra between 3.3 and 3.45 μm are ascribed to the CH_3 functional groups while the peak between 3.45–3.5 μm is due to the CH_2 functional group[28]. Note that the AHS reflectance peaks are slightly broader in comparison to that of the FTIR. This is due to the relatively low spectral resolution of the FPI. Similarly, the FTIR and AHS reflectance spectra of black PE500 are compared in Fig. 4b.

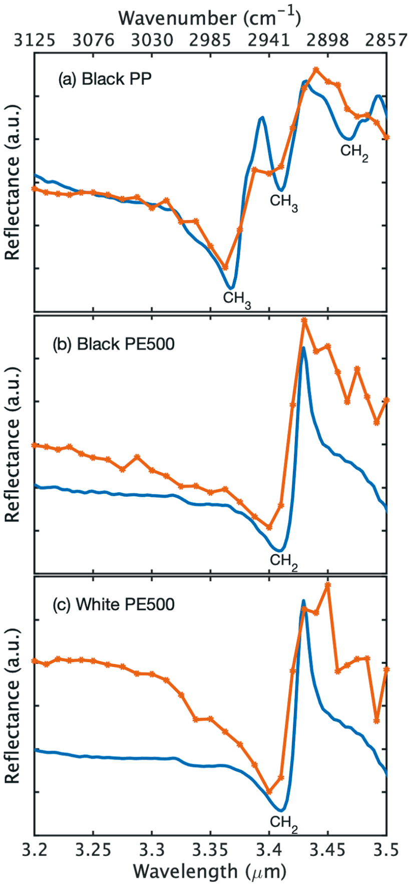

Figure 4. (**a**), (**b**) and (**c**) compares the reflectance spectra of black polypropylene (PP), black polyethylene (PE500) and white polyethylene (PE500), respectively. Solid blue line represents the spectra measured with FTIR spectrometer and the red line with a marker represents that of the active hyperspectral sensor (AHS).

Both spectra are in excellent agreement as shown in the figure. The reflectance peak between 3.4–3.45 μm spectral region is assigned to the CH_2 functional group. Although both black PP and PE500 have somewhat similar spectral absorption features, their reflectance spectra are clearly distinguishable as shown in Fig. 4a, b respectively.

The AHS is further extended to the measurement of white plastics to ascertain the reliability of the technique as well as the impact of the additive coloring material. Fig. 4c presents a comparison between AHS and FTIR reflectance spectra of a white PE500. We can see a very good agreement between them. Moreover, the reflectance spectra of both the black and the white PE500 are very similar as can be seen in Fig. 4b,c, respectively. This is because the additive coloring material has negligible impact on the optical properties of the polymer at this wavelength range. This highlights the potential applicability of the sensor to differently colored plastics. There is a slight variation in the AHS spectra of the plastics. The cause for this is attributed to the fact that samples used in this work vary in surface quality (glossy, matte or rough surface), which leads to different light scattering properties. Nonetheless, all the absorption peaks are clearly present in the measured spectra and can be used for the identification and differentiation of the plastic species.

Conclusion

We developed a novel hyperspectral sensor using a mid-infrared supercontinuum light source and a tunable MEMS-based Fabry-Pérot interferometer. The FPI enables robust wavelength selection across the probed spectral range of the SC spectrum. The FPI is engineered to be standalone, thereby enabling robust sensor design as positioning of the FPI on the sensor is flexible. For instance, placing the FPI in front of the laser would allow target illumination with only the desired spectral components with relatively low power compared to the whole SC spectrum, this is particularly important in applications where the target sample has very low damage threshold. Our preliminary demonstration of line filtering with a FPI of similar principal mechanism operating in the near infrared, with an aperture size of about 1.5 mm, showed a power handling of more than 10 W of continuous wave of a 1–2 μm SC laser. We demonstrated hyperspectral sensing of black polyethylene (PE500) and polypropylene (PP) using the 3–3.5 μm band of the SC spectrum. The measured reflectance spectra of the plastics are compared to their reference measured with an FTIR spectrometer. An excellent agreement was observed between the spectra. Furthermore, we measured the reflectance spectra of a white PE500 to emphasize the applicability of the sensor to differently colored plastic samples. Our results showed, for the first time, the suitability of the FPI for active hyperspectral identification of polymers. The sensor demonstrates a measurement rate of about sixty-five spectra per second, limited by the tuning frequency of the FPI, and a relative intensity noise of 1–8 % in the 3–3.5 μm wavelength range. The main sources of noise in this work are the supercontinuum light source spectrum instabilities and the readout noise associated with the detector, amplifier as well as the FPGA. It is important to emphasize that the measurement speed and accuracy can be significantly improved by optimizing the 0.5 duty cycle scanning frequency of the Fabry-Pérot interferometer to make use of the full cycle, which would double the spectrum acquisition rate and enhance the signal level during the same acquisition time, and thus increase the signal-to-noise ratio by a factor of $\sqrt{2}$. Further improvement can be achieved by tailoring temporal scanning profile so that noisy part of the spectrum would have longer integration time compared to other parts of the spectrum. Furthermore, the biggest improvement can be realized by using better tailored supercontinuum light source where the wavelength range of interest is not located at the far edge of the SC spectrum. This would result in increase of average spectral density in that region, and significantly decrease shot to shot fluctuations thereby enhancing the signal-to-noise ratio of measured spectra. The aforementioned optimizations would enable real-time plastic wastes sorting and other hyperspectral sensing applications in the mid-infrared.

Data availibility

The datasets used and/or analysed during the current study are available from the corresponding author upon reasonable request.

Received: 29 June 2022; Accepted: 4 November 2022
Published online: 12 November 2022

References

1. Adão, T. *et al.* Hyperspectral imaging: A review on uav-based sensors, data processing and applications for agriculture and forestry. *Remote Sens.* **9**, 1110 (2017).
2. Lu, G. & Fei, B. Medical hyperspectral imaging: A review. *J. Biomed. Opt.* **19**, 010901 (2014).
3. Krupnik, D. & Khan, S. Close-range, ground-based hyperspectral imaging for mining applications at various scales: review and case studies. *Earth Sci. Rev.* **198**, 102952 (2019).
4. Dudley, J. M., Genty, G. & Coen, S. Supercontinuum generation in photonic crystal fiber. *Rev. Mod. Phys.* **78**, 1135 (2006).
5. Genty, G., Coen, S. & Dudley, J. M. Fiber supercontinuum sources. *JOSA B* **24**, 1771–1785 (2007).
6. Saleh, A., Aalto, A., Ryczkowski, P., Genty, G. & Toivonen, J. Short-range supercontinuum-based lidar for temperature profiling. *Opt. Lett.* **44**, 4223–4226 (2019).
7. Saleh, A., Ryczkowski, P., Genty, G. & Toivonen, J. Supercontinuum lidar for industrial process analysis. *Opt. Express* **29**, 42082–42089 (2021).
8. Kilgus, J., Duswald, K., Langer, G. & Brandstetter, M. Mid-infrared standoff spectroscopy using a supercontinuum laser with compact fabry-pérot filter spectrometers. *Appl. Spectrosc.* **72**, 634–642 (2018).
9. Kääriäinen, T., Jaanson, P., Vaigu, A., Mannila, R. & Manninen, A. Active hyperspectral sensor based on mems fabry-pérot interferometer. *Sensors* **19**, 2192 (2019).
10. Kääriäinen, T. & Dönsberg, T. Active hyperspectral imager using a tunable supercontinuum light source based on a mems fabry-perot interferometer. *Opt. Lett.* **46**, 5533–5536 (2021).
11. Petersen, C. R. *et al.* Mid-infrared supercontinuum covering the 1.4–13.3 μm molecular fingerprint region using ultra-high na chalcogenide step-index fibre. *Nat. Photonics* **8**, 830–834 (2014).
12. Zhao, Z. *et al.* Mid-infrared supercontinuum covering 2.0–16 μm in a low-loss telluride single-mode fiber. *Laser Photonics Rev* **11**, 1700005 (2017).
13. Liu, K., Liu, J., Shi, H., Tan, F. & Wang, P. High power mid-infrared supercontinuum generation in a single-mode zblan fiber with upto 21.8 w average output power. *Opt. Express* **22**, 24384–24391 (2014).
14. Kedenburg, S. *et al.* High repetition rate mid-infrared supercontinuum generation from 1.3 to 5.3 μm in robust step-index tellurite fibers. *JOSA B* **34**, 601–607 (2017).
15. Salem, R. *et al.* Mid-infrared supercontinuum generation spanning 1.8 octaves using step-index indium fluoride fiber pumped by a femtosecond fiber laser near 2 μm. *Opt. Express* **23**, 30592–30602 (2015).
16. Eslami, Z., Ryczkowski, P., Salmela, L. & Genty, G. Low-noise octave-spanning mid-infrared supercontinuum generation in a multimode chalcogenide fiber. *Opt. Lett.* **45**, 3103–3106 (2020).
17. Mikkonen, T. *et al.* Broadband cantilever-enhanced photoacoustic spectroscopy in the mid-ir using a supercontinuum. *Opt. Lett.* **43**, 5094–5097 (2018).
18. Petersen, C. R. *et al.* Mid-infrared multispectral tissue imaging using a chalcogenide fiber supercontinuum source. *Opt. Lett.* **43**, 999–1002 (2018).
19. Zorin, I. *et al.* Mid-infrared fourier-domain optical coherence tomography with a pyroelectric linear array. *Opt. Express* **26**, 33428–33439 (2018).
20. Hollas, J. M. *Modern Spectroscopy* (John Wiley & Sons, 2004).
21. Signoret, C., Caro-Bretelle, A.-S., Lopez-Cuesta, J.-M., Ienny, P. & Perrin, D. Mir spectral characterization of plastic to enable discrimination in an industrial recycling context: I. Specific case of styrenic polymers. *Waste Manag.* **95**, 513–525 (2019).
22. Rissanen, A. *et al.* Vtt's fabry-perot interferometer technologies for hyperspectral imaging and mobile sensing applications. . In *Moems and Miniaturized Systems Xvi* Vol. 10116. pp. 119–130 (International Society for Optics and Photonics, 2017).
23. Akujärvi, A., Guo, B., Mannila, R. & Rissanen, A. Moems fpi sensors for nir-mir microspectrometer applications. In *Moems and Miniaturized Systems Xv* Vol. 9760. pp. 117–124 (International Society for Optics and Photonics, 2016).

24. Rissanen, A., Akujärvi, A., Antila, J. E., Blomberg, M. & Saari, H. K. MOESMs miniature spectrometers using tuneable fabry-perot interferometers. *J. Micro/Nanolithogr. MEMS MOEMS* **11**, 023003 (2012).
25. Rissanen, A., Mannila, R., Tuohiniemi, M., Akujärvi, A. & Antila, J. Tunable moems fabry-perot interferometer for miniaturized spectral sensing in near-infrared. in *MOEMS and Miniaturized Systems XIII* Vol. 8977. pp. 243–250 (International Society for Optics and Photonics, 2014).
26. Amiot, C., Aalto, A., Ryczkowski, P., Toivonen, J. & Genty, G. Cavity enhanced absorption spectroscopy in the mid-infrared using a supercontinuum source. *Appl. Phys. Lett.* **111**, 061103 (2017).
27. Kudlinski, A. *et al.* Control of pulse-to-pulse fluctuations in visible supercontinuum. *Opt. Express* **18**, 27445–27454 (2010).
28. Becker, W., Sachsenheimer, K. & Klemenz, M. Detection of black plastics in the middle infrared spectrum (MIR) using photon up-conversion technique for polymer recycling purposes. *Polymers* **9**, 435 (2017).

Acknowledgements

A.S. acknowledges the support from Finnish Foundation for Technology Promotion, and Finnish Cultural Foundation. The authors also acknowledge Academy of Finland (Flagship PREIN, 320165).

Author contributions

A.S. conducted the experiments. J.T. and G.G. supervised the project. All authors contributed to the data analysis and writing of the manuscript.

Competing interests

The authors declare no competing interests.

Additional information

Correspondence and requests for materials should be addressed to A.S.

Reprints and permissions information is available at www.nature.com/reprints.

Publisher's note Springer Nature remains neutral with regard to jurisdictional claims in published maps and institutional affiliations.

Open Access This article is licensed under a Creative Commons Attribution 4.0 International License, which permits use, sharing, adaptation, distribution and reproduction in any medium or format, as long as you give appropriate credit to the original author(s) and the source, provide a link to the Creative Commons licence, and indicate if changes were made. The images or other third party material in this article are included in the article's Creative Commons licence, unless indicated otherwise in a credit line to the material. If material is not included in the article's Creative Commons licence and your intended use is not permitted by statutory regulation or exceeds the permitted use, you will need to obtain permission directly from the copyright holder. To view a copy of this licence, visit http://creativecommons.org/licenses/by/4.0/.

© The Author(s) 2022

PUBLICATION
IV

In-situ analysis of combustion aerosol using a supercontinuum lidar

A. Saleh, K. Kalmankoski, G. Genty and J. Toivonen

Optics Express 31.15 (2023), pp. 23889–23896

DOI: 10.1364/OE.492715

Publication is licensed under a Creative Commons Attribution 4.0 International License CC-BY-NC-ND

Research Article Vol. 31, No. 15 / 17 Jul 2023 / *Optics Express* 23889

Optics EXPRESS

In-situ analysis of combustion aerosol using a supercontinuum lidar

ABBA SALEH,* KIM KALMANKOSKI, GOËRY GENTY, AND JUHA TOIVONEN

Photonics Laboratory, Physics Unit, Tampere University, P.O. Box 692, FI-33101 Tampere, Finland
**abba.saleh@tuni.fi*

Abstract: We report real-time monitoring of coarse aerosol particle distribution in a 9 m wide full-scale industrial boiler using a broadband supercontinuum lidar. The technique utilizes the light backscattered from the aerosol to map the extinction profile using the Klett inversion method, with measured extinction values of $0.04 - 0.2\,\mathrm{m}^{-1}$ across the furnace. The technique further exploits differential absorption of water molecules in the $1.25 - 1.5\,\mu\mathrm{m}$ region to map the water vapor concentration profile in the furnace up to a distance of 3.9 m with a spatial resolution of 30 cm. We also take advantage of the strong reflection from the boiler back-wall to simultaneously measure the average water vapor temperature and concentration in the boiler in good agreement with reference readings from the boiler. Our results open novel perspectives for versatile 3D profiling of flue gas parameters and other industrial process analysis.

Published by Optica Publishing Group under the terms of the Creative Commons Attribution 4.0 License. Further distribution of this work must maintain attribution to the author(s) and the published article's title, journal citation, and DOI.

1. Introduction

Owing to its CO_2 neutrality, biomass has gained significant attention as an alternative sustainable source of energy and it is nowadays widely used as renewable fuel in combustion power plant boilers. However, the exact composition of biomass can vary significantly such that optimal performance of the combustion process generally requires dynamic monitoring of the flue gas parameters, including temperature, molecular concentrations and fly ash aerosol particles. Aerosol particles can further act as contaminants which may cause malfunction in the combustion unit. For example, alkali chloride salt particles, such as KCl and CaCl, naturally produced during the combustion process can deposit on the surface of heat exchangers or other critical components of the combustion unit, and their reaction with these surfaces often leads to corrosion [1–3] and fouling [4–6]. This in turn can critically affect the convective heat transfer essential for the combustion process. Additionally, the aerosol size distribution and concentration can yield important information regarding the boiler bed conditions [7] as well as the fuel quality [8].

The conventional approach to monitor combustion aerosols relies on extracting the aerosol particles from the combustion unit via a suction tube to a designated measurement device [9,10]. A similar technique is also used to measure the molecular concentration of probed gases [11,12]. This approach however poses significant challenges such as latency, condensation in the tubes and possible nucleation or coagulation of the particles, complicating real-time probing of the flue gas parameters. Alternative methods based on optical spectroscopy [13–17] have been introduced for gas-phase reaction studies in combustion applications, but they require at least two openings on the furnace walls as they measure the transmitted signal through a particular area. This makes their application to combustion units with limited openings, such as boilers, unpractical. Techniques based on light detection and ranging (lidar) that are based on reflected light do not require multiple opening and are particularly adapted to remote measurement of flue gas parameters [18–20]. These techniques however are limited to probing one flue gas component at a time. Recently, we have introduced a new lidar system employing a broadband

#492715 https://doi.org/10.1364/OE.492715
Journal © 2023 Received 12 Apr 2023; revised 9 Jun 2023; accepted 13 Jun 2023; published 5 Jul 2023

supercontinuum light source capable of simultaneously probing the flue gas temperature and molecular concentration in an industrial boiler [21,22].

Herein, we expand this recent work and demonstrate a supercontinuum lidar (SC-lidar) system capable of simultaneously monitoring the spatially-resolved aerosol particle distribution and measuring the water vapor (H_2O) temperature and concentration in an industrial power plant boiler via a single measurement port. The technique exploits differential absorption between three specific spectral channels in the SC spectrum (Ch1, Ch2 and Ch3 in Fig. 1). Specifically, we map the coarse aerosol particle distribution along the beam path from the signal backscattered by the aerosol particles at SC wavelengths not absorbed in the boiler, and we characterize the water vapor concentration distribution in the furnace up to a distance of 3.9 m by exploiting differential absorption in the SC spectrum. Finally, the average water vapor temperature and concentration in the boiler are obtained from the strong backscattered light from the back-wall of the boiler. Our results highlights the unique potential of the SC-lidar for real-time versatile sensing and process analysis in industrial environments.

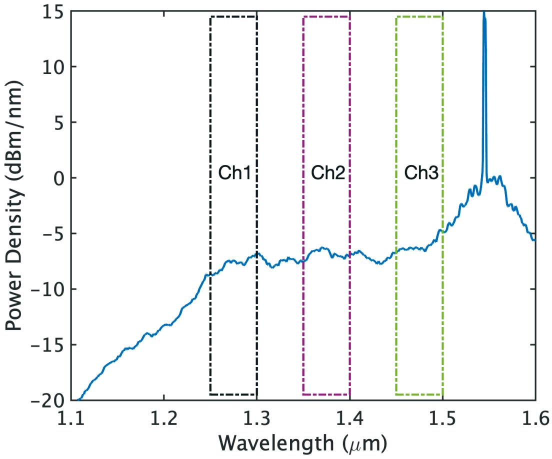

Fig. 1. Power spectral density of the supercontinuum light source with the corresponding full width at half maximum of the SC-lidar spectral channels indicated by the rectangles.

2. Aerosol extinction estimation

The measured extinction coefficient α of a lidar beam generally depends both on the absorption by gaseous species α_{abs} and scattering by aerosol particles α_{sca}, such that $\alpha = \alpha_{abs} + \alpha_{sca}$. The aerosol extinction is generally wavelength dependent especially in Rayleigh and Mie regime. However, considering homogeneous composition of aerosols dominated by coarse particles in the furnace and relatively narrow band of the SC-lidar spectral channels, α_{sca} is mainly proportional to the particle volume fraction on the beam path. In order to obtain the extinction coefficient from a measurement, we begin by including the α_{sca} into the known lidar equation for broad band SC source [22]:

$$S_n(R) = \beta(R)\frac{O(R)}{R^2}\int_{\Delta\lambda_n} P_0(\lambda)\Gamma_n(\lambda)e^{-2\int_0^R \alpha_{abs}(\lambda,T,R') + \alpha_{sca}(R')\,dR'}\,d\lambda, \tag{1}$$

where n denotes the spectral channel and R is the measurement distance. The detected signal is proportional to the aerosol backscattering coefficient $\beta(R)$ and $O(R)$ is the geometrical form factor accounting for the fraction of backscattered signal from a distance R which is effectively detected. $P_0(\lambda)$ is the power spectrum of the SC light source and $\Gamma_n(\lambda)$ is the filter transmission for a given channel n. The absorption effect on extinction can be neglected for spectral channels which are outside the absorption wavelength range (Ch1 in our case). Therefore, Eq. (1) reduces to

$$S_1(R) = \beta(R)\frac{O(R)}{R^2}P_1 e^{-2\int_0^R \alpha(R')\,dR'}, \tag{2}$$

where $P_1 = \int_{\Delta\lambda_n} P_0(\lambda)\Gamma_1(\lambda)\,d\lambda$. Note that for a homogeneous aerosol mixture $\beta = L\alpha$ [23], where L is the ratio of aerosol specific backscattering coefficient to the extinction coefficient. Eq. (2) is analogous to the typical elastic backscatter lidar equation, thus, the aerosol distribution in the furnace can be estimated by solving for the extinction coefficient using the inversion method introduced by Klett [23,24]. The method is widely used in atmospheric lidar applications due to its stability and tolerance to noise [25]. The method involves estimating the extinction coefficient in a reference distance using

$$\alpha(R) = \frac{e^{W(R)-W(R_m)}}{\frac{1}{\alpha(R_m)} + 2\int_R^{R_m} e^{W(R')-W(R_m)}\,dR'}, \tag{3}$$

where W is a logarithmic range corrected signal ($ln[\frac{S_1(R)R^2}{O(R)}]$), R_m is a chosen reference distance such that $R<R_m$. One can also estimate the initial values of extinction at a given reference distance by a simple slope method suggested by Klett as $\alpha(R_m) = \frac{1}{2}\frac{W_0-W_m}{R_m-R_0}$, where the zero subscript denotes the starting point of the slope. This means that knowing the aerosol backscattered signal Ch1, the geometrical form factor and the measurement distance is sufficient to estimate the extinction coefficient.

3. Experiment

The supercontinuum is generated by injecting sub-nanosecond pulses at 1547 nm from a gain-switched fiber laser (Keopsys-PEFL-K09) producing 10 kW peak power at 100 kHz repetition rate into the anomalous dispersion regime of a 30-cm-long silica dispersion-shifted fiber (DSF, Corning, Inc. LEAF) with zero dispersion wavelength (ZDW) at 1510 nm followed by a 3-m-long dispersion compensating fiber (DCF4, Thorlabs) with ZDW at 1583 nm. The 1510 nm zero dispersion wavelength (ZDW) of the DSF enables noise-seeded modulation instability, breaking up the long pump pulses into a large number of solitons. Subsequent propagation in the dispersion compensating fiber allows for soliton dynamics for wavelengths above 1583 nm (including dispersive wave generation, Raman self-frequency shift and cross-phase modulation) yielding efficient energy transfer in the 1.1-1.6 microns region. The resulting SC spectrum covers 0.8 – 2.4 µm up to the silica transparency window. The output SC pulses have the same pulse parameters as the input pump pulses. Fig. 1 shows the SC power spectral density in the 1.1 – 1.6 µm spectral range of interest for our experiments. The full width at half maximum (FWHM) of the bandpass filters used as spectral channels for the lidar measurements are also marked in the figure.

The lidar measurements were conducted in a 9-m-wide bubbling fluidized bed (BFB) biomass boiler with thermal power of 190 MW. A schematic illustration of the experimental setup is shown in the inset in Fig. 2. The setup is similar to that in Ref. 22 except for the bandpass filters associated with the three spectral channels, which are different (87-852, 87-867 & 87-856, Edmund Optics) and are specifically selected to ensure optimal coverage of the differently absorbing spectral channels. The setup also includes a field programmable gate array (FPGA) board (EK-U1-ZCU111-G, Xlinx) which utilizes the built-in 12-bit analog-to-digital converter to digitize the signals after the amplifier at a sampling rate of 4 GHz. This process is repeated iteratively averaging up to 3 x 10^5 signals per individual channel over a total measurement time of 3 s. Constant measurement time and averaging was used in all measurements. Figure 2 shows an example of recorded signal where we can identify three distinct peaks at different delay times. The first peak near −10 ns represents scattering from the coupling mirror placed in front of the receiver optics. The backscattered signal from the aerosol particles corresponds to the broad skewed peak starting at 0 ns and the peak around 60 ns originates from the boiler back-wall reflection.

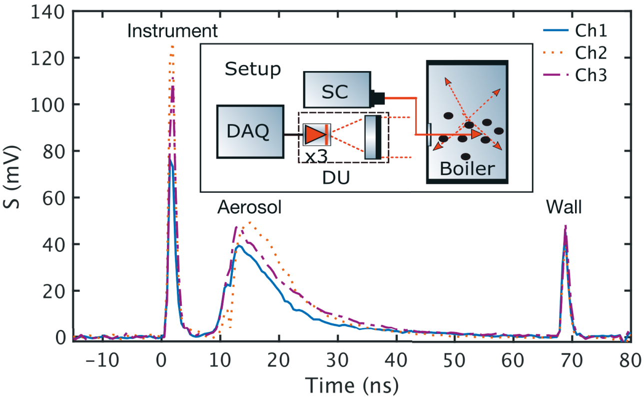

Fig. 2. Measured SC-lidar signal from a full-scale industrial boiler. Ch1 (solid line), Ch2 (dotted line) and Ch3 (dashed line) represents the signal from the three specific spectral channels used in the supercontinuum spectrum. Inset is the corresponding experimental setup. DU: detection unit, DAQ: data acquisition.

4. Results

The aerosol distribution in the furnace can be retrieved from the Ch1 backscattered signal, which corresponds to the spectral channel with negligible absorbance in the beam path, where the extinction in the lidar beam is mainly due to scattering by the aerosol particles. The geometrical form factor $O(R)$ is evaluated by continuously displacing a diffusing hard target over a given distance R, and measuring the backscattered signal multiple times. The measurement was done outside of the boiler furnace to exclude aerosol extinction effect inside the boiler. A polynomial piece-wise fitting is applied to obtain a continuous form factor function that applies to all data points. The form factor and measurement distance are used to cancel out the geometrical effect on the signal. Figure 3 shows the range corrected signal (solid blue line) and the corresponding geometrical form factor of our SC-lidar system (dashed red line). The initial values for extinction are calculated using $R_0 = 1\,m$ and $R_m = 8\,m$, representing an interval with adequate signal-to-noise ratio (SNR) and a clear slope in the logarithmic range corrected signal W. The extinction values are extracted using the resulting initial values in Eq. (3), and the corresponding extinction map is shown in the lower panel in Fig. 4. It represents a 90 s extinction time series across the furnace. The 90 s time window is arbitrarily selected with respect to the furnace operational timeline. The resulting extinction values imply a dynamic concentration distribution of the aerosol particles. The extinction values at 1 – 2 m distance in the furnace slightly fluctuates around 0.1 m^{-1} over time, with a standard deviation of 0.01m^{-1}, corresponding to a relatively moderate concentration of the aerosol particles. The variation in the extinction values (i.e. the distribution of the aerosol particles concentration) becomes more pronounced at longer distances, with extinction values in the range of $0.04 - 0.2\,m^{-1}$. The inhomogeneous aerosol concentration distribution in the furnace can be attributed to the air feed for the combustion process, due to the correlation between air flow and particle distribution. This in turn could be exploited to complement flow measurements in the furnace. Further analysis of the aerosol concentration distribution can also yield information regarding the fuel quality [8]. Finally, optimizing the SC-lidar to enable particle size distribution analysis would pave the way for monitoring the boiler bed conditions [7]. This can be achieved using multi-octave spanning broadband light sources.

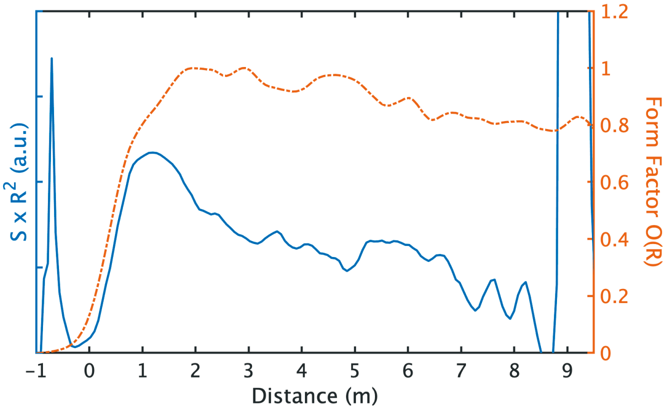

Fig. 3. Measured Ch1 range corrected signal (solid line) and the corresponding geometrical form factor of the SC-lidar (dashed line). The bang in the corrected signal at around 9 m originates from the boiler back wall reflection.

Analysis of temperature and molecular concentrations also plays a central role in the optimization of the combustion processes as aforementioned in the introduction section. To map out temperature and molecular concentrations in the furnace, one can further utilize the backscattered signal from the aerosol particles in spectral channels corresponding to the absorption region of H_2O (which is one of the primary flue gas component with rich absorption spectrum in the infrared). Specifically, variations in H_2O concentration were obtained from the backscattered signal from the aerosol particles in spectral channels Ch1 and Ch2 and using a reference temperature value of 850 °C in Eq. 3 of Ref. 22. The H_2O concentration profile along the beam path could be resolved up to a distance of 3.9 m as shown in Fig. 5, limited by the SNR of our measurement. The SNR also restricts mapping of temperature variation in the furnace, as the temperature induced relative change in the backscattered signal intensity is comparable to the noise amplitude of the recorded data. In this respect, the detector, amplifier and FPGA associated readout noise as well as the supercontinuum source spectral instabilities are currently the main sources of noise in this experiment. In order to enhance the SNR and increase the probing distance of our lidar system, there are several improvements which could be implemented. These include increasing the continuous averaging during the detection, using a detector with better noise performance, or using a supercontinuum with higher power spectral density and lower relative intensity noise.

Nonetheless, one can also exploit the strong instrument and back-wall reflection in the SC-lidar signal in Fig. 2 to extract both the average H_2O temperature and concentration in the furnace

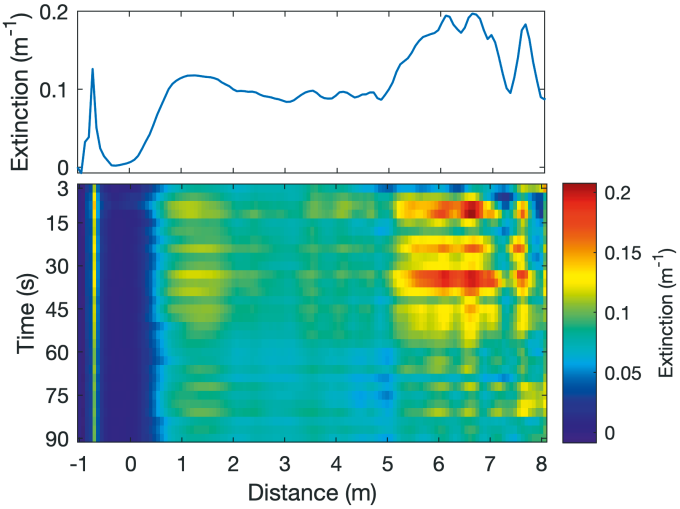

Fig. 4. Bottom panel: measured extinction profile of the coarse aerosol particles in the boiler over 30 consecutive measurements with a corresponding total measurement time of 90 s. Top panel: an example of a single measurement from the time series extinction map.

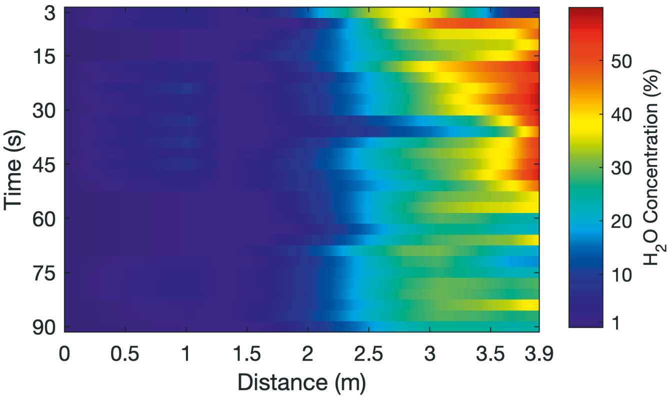

Fig. 5. Measured water vapor concentration variation in the boiler over 30 consecutive measurements with a corresponding total measurement time of 90 s.

by simultaneously solving for Eq. (3) and Eq. (4) of Ref. 22. This yields values of 830 °C and 20.6 % for average H_2O temperature and concentration, respectively, in very good agreement with the reference temperature value of 850 °C (measured with a K-type thermocouple) and concentration in the range 20 – 25 % (estimated based on heat and mass balance calculations [26]). It is also important to emphasize that the results are consistent with earlier reported values [22] appropriate for industrial process analysis.

5. Conclusion

We have reported proof-of-concept demonstration of in-situ combustion diagnostics in a full-scale industrial boiler using a broadband supercontinuum lidar system via a single optical access. The technique utilizes three specific wavelength bands in the supercontinuum spectrum, which enables versatile analysis of flue gas parameters. With this approach, we have demonstrated spatially-resolved remote measurement of coarse aerosol particle distribution in the boiler, with extinction values in the range of $0.04 - 0.2\,\mathrm{m}^{-1}$. Our result can be used to complement flow measurements in the furnace due to the correlation between air flow and particle distribution. Average water vapor temperature and concentration in the furnace is also measured with accuracy consistent with earlier reported values [22] and appropriate for industrial process monitoring. We also mapped the water vapor concentration profile up to 3.9 m distance inside the boiler, limited by the signal-to-noise ratio (SNR) of our detection system. A higher SNR would enhance the probing distance and in principle enable spatially resolving the gas temperature. In the future, we believe that supercontinuum-based lidar systems can be further expanded to perform full 3D mapping of flue gas parameters in combustion environments and other versatile industrial process monitoring, by steering the incident probe beam using a special mirror arrangement or other advanced micro-electro-mechanical systems (MEMS).

Funding. Academy of Finland (320165).

Acknowledgments. A.S acknowledges the support from Finnish Foundation for Technology Promotion. The authors are sincerely grateful to Jaani Silvennoinen and Jari Perälä for organizing the measurement campapaign, and Tampereen Sähkölaitos for making their power plant accessible and the hospitality.

Disclosures. The authors declare no conflicts of interest.

Data availability. Data underlying the results presented in this paper are not publicly available at this time but may be obtained from the authors upon reasonable request.

References

1. R. A. Antunes and M. C. L. de Oliveira, “Corrosion in biomass combustion: A materials selection analysis and its interaction with corrosion mechanisms and mitigation strategies,” Corros. Sci. **76**, 6–26 (2013).
2. H. P. Nielsen, F. Frandsen, K. Dam-Johansen, and L. Baxter, “The implications of chlorine-associated corrosion on the operation of biomass-fired boilers,” Prog. Energy Combust. Sci. **26**(3), 283–298 (2000).
3. E. Vainio, N. DeMartini, L. Hupa, L.-E. Åmand, T. Richards, and M. Hupa, “Hygroscopic properties of calcium chloride and its role on cold-end corrosion in biomass combustion,” Energy Fuels **33**(11), 11913–11922 (2019).
4. M. Theis, B.-J. Skrifvars, M. Hupa, and H. Tran, “Fouling tendency of ash resulting from burning mixtures of biofuels. part 1: Deposition rates,” Fuel **85**(7-8), 1125–1130 (2006).
5. B.-J. Skrifvars, P. Yrjas, T. Laurén, J. Kinni, H. Tran, and M. Hupa, “The fouling behavior of rice husk ash in fluidized-bed combustion. 2. pilot-scale and full-scale measurements,” Energy Fuels **19**(4), 1512–1519 (2005).
6. A. F. Stam, K. Haasnoot, and G. Brem, “Superheater fouling in a bfb boiler firing wood-based fuel blends,” Fuel **135**, 322–331 (2014).
7. B.-Å. Andersson, “Effects of bed particle size on heat transfer in circulating fluidized bed boilers,” Powder Technol. **87**(3), 239–248 (1996).
8. A. Garcia-Maraver, M. Zamorano, U. Fernandes, M. Rabaçal, and M. Costa, “Relationship between fuel quality and gaseous and particulate matter emissions in a domestic pellet-fired boiler,” Fuel **119**, 141–152 (2014).
9. E. Gustafsson, L. Lin, M. C. Seemann, J. Rodin, and M. Strand, “Characterization of particulate matter in the hot product gas from indirect steam bubbling fluidized bed gasification of wood pellets,” Energy Fuels **25**(4), 1781–1789 (2011).
10. H. Kuuluvainen, P. Karjalainen, C. J. Bajamundi, J. Maunula, P. Vainikka, J. Roppo, J. Keskinen, and T. Rönkkö, “Physical properties of aerosol particles measured from a bubbling fluidized bed boiler,” Fuel **139**, 144–153 (2015).
11. E. Vainio, A. Brink, M. Hupa, H. Vesala, and T. Kajolinna, “Fate of fuel nitrogen in the furnace of an industrial bubbling fluidized bed boiler during combustion of biomass fuel mixtures,” Energy Fuels **26**(1), 94–101 (2012).
12. E. Vainio, *Fate of fuel-bound nitrogen and sulfur in biomass-fired industrial boilers* (Åbo Akademi University, PhD thesis, 2014).
13. T. Sorvajärvi, N. DeMartini, J. Rossi, and J. Toivonen, “In situ measurement technique for simultaneous detection of k, kcl, and koh vapors released during combustion of solid biomass fuel in a single particle reactor,” Appl. Spectrosc. **68**(2), 179–184 (2014).
14. X. Zhou, J. Jeffries, and R. Hanson, “Development of a fast temperature sensor for combustion gases using a single tunable diode laser,” Appl. Phys. B **81**(5), 711–722 (2005).

15. M. Aldén, A. Omrane, M. Richter, and G. Särner, "Thermographic phosphors for thermometry: a survey of combustion applications," Prog. Energy Combust. Sci. **37**(4), 422–461 (2011).
16. J. Borggren, W. Weng, A. Hosseinnia, P.-E. Bengtsson, M. Aldén, and Z. Li, "Diode laser-based thermometry using two-line atomic fluorescence of indium and gallium," Appl. Phys. B **123**(12), 278 (2017).
17. J. Viljanen, T. Sorvajärvi, and J. Toivonen, "In situ laser measurement of oxygen concentration and flue gas temperature utilizing chemical reaction kinetics," Opt. Lett. **42**(23), 4925–4928 (2017).
18. B. Kaldvee, J. Bood, and M. Aldén, "Picosecond-lidar thermometry in a measurement volume surrounded by highly scattering media," Meas. Sci. Technol. **22**(12), 125302 (2011).
19. E. Malmqvist, J. Borggren, M. Aldén, and J. Bood, "Lidar thermometry using two-line atomic fluorescence," Appl. Opt. **58**(4), 1128–1133 (2019).
20. E. Malmqvist, M. Brydegaard, M. Aldén, and J. Bood, "Scheimpflug lidar for combustion diagnostics," Opt. Express **26**(12), 14842–14858 (2018).
21. A. Saleh, A. Aalto, P. Ryczkowski, G. Genty, and J. Toivonen, "Short-range supercontinuum-based lidar for temperature profiling," Opt. Lett. **44**(17), 4223–4226 (2019).
22. A. Saleh, P. Ryczkowski, G. Genty, and J. Toivonen, "Supercontinuum lidar for industrial process analysis," Opt. Express **29**(25), 42082–42089 (2021).
23. J. D. Klett, "Lidar inversion with variable backscatter/extinction ratios," Appl. Opt. **24**(11), 1638 (1985).
24. J. D. Klett, "Stable analytical inversion solution for processing lidar returns," Appl. Opt. **20**(2), 211 (1981).
25. A. Comerón, C. Mu noz-Porcar, F. Rocadenbosch, A. Rodríguez-Gómez, and M. Sicard, "Current Research in Lidar Technology Used for the Remote Sensing of Atmospheric Aerosols," Sensors **17**(6), 1450 (2017).
26. K. C. Weston, "Energy conversion. chapter 3: Fuels and combustion," (1992).

130.230.127.221 {ts '2023-07-10 08:07:50'}